A Mechanism for Simplified Scanner Control with Application to MRI-guided Interventions

By Matthew A. MacDonald

A Thesis Presented to Lakehead University in Partial Fulfillment of the Requirement for the Degree of

Master of Science in Electrical and Computer Engineering

Abstract

Matthew A. MacDonald. A Mechanism for Simplified Scanner Control with Application to MRI-guided Interventions (Under the Supervision of Dr. Samuel Pichardo).

Magnetic Resonance Image (MRI)-guided interventions involving percutaneous biopsies of lesions, or trajectory alignment with prospective stereotaxy are conducted in real time using rapid image acquisition. A mechanism of passively localizing a device and calculating its orientation is desired to improve interventional outcomes in these situations. In this work, we propose and evaluate an image-based technique to determine the position and alignment of a linearly shaped interventional device within an *ex-vivo* tissue specimen. Low resolution 3D orientation scan data is processed to produce a virtual line fitting using principal component analysis. The line fitting algorithm was incorporated into a biopsy needle tracking system implemented with an MR-scanner operated using a footswitch. A GUI application was written to collect foot pedal input and display automated visualization of device placement inside the scanner room. Placement time trials (N=3) conducted with this system using porcine muscle and phantom samples suspended in rigid frames with inserted gadolinium-enhanced targets. The mean targeting error across all directions was 3.6 mm and 5.1 mm for the phantom trials and *ex-vivo* trials respectively. The average entry-to-target time was 247 sec. Device localization during trials was adequate to contain a 11-gauge titanium biopsy needle within a visualization slice volume of 10 mm after 93.8% of alignments over insertion lengths between 30 mm to 110 mm at insertion angles between $1.4°$ to $20°$ from the static magnetic field and frequency encoding axes. Practical considerations were identified and occupational exposure measurements were collected as part of determining the system's overall feasibility.

Biographical Summary

Matthew A. MacDonald was born in 1985 in Scarborough, Ontario, Canada. After completing an advanced diploma with honors in Electronics Engineering Technology at Seneca College, he was the only student to have ever completed an Ontario Graduate Certificate in Seneca's Applied Electronic Design program without first graduating from university and was additionally awarded high honors. After working as an analyst for Scotia Capital in Toronto, he completed a Bachelor's Degree in Electrical Engineering at Lakehead University with First Class standing. He has since conducted research at the Thunder Bay Regional Research Institute as an assistant to Dr. Samuel Pichardo while completing his thesis work in Lakehead University's Master of Science in Electrical and Computer Engineering program. He has been awarded the Natural Sciences and Engineering Council of Canada's Canadian Graduate Scholarship as well as an Ontario Graduate Scholarship to complete this work.

Acknowledgments

Contents

Appendices   **67**

A   **68**

List of Figures

List of Tables

List of Symbols

α	–	RF excitation flip angle (°).
α_E	–	Ernst angle (°).
a	–	Average number of realignments.
β	–	Angle of device axis from the direction of frequency encoding (°).
$\hat{\mathbf{b}}$	–	Scan plane row unit vector.
$\frac{dB}{dt}$	–	Rate of change of the gradient coil magnetic flux density $(\mathrm{T} \cdot \mathrm{s}^{-1})$.
B_0	–	Static magnetic field strength (T).
BW_{RF}	–	RF excitation pulse bandwidth (Hz).
BW_f	–	Frequency encoding signal bandwidth (Hz).
BW_p	–	Phase encoding signal bandwidth (Hz).
$\mathbf{C}$	–	Covariance matrix.
c	–	PNS chronaxie time (ms).
δ	–	Angle of device axis from that of the static magnetic field (°).
$\hat{\mathbf{d}}$	–	Scan plane column unit vector.
d	–	Biopsy needle outer diameter (mm).
ϵ	–	Localization positional error in the slice-selection direction (mm).
Δf	–	Precession frequency shift (Hz).
f	–	Factor score.
γ	–	Gyromagnetic ratio $(\mathrm{Hz} \cdot \mathrm{T}^{-1})$.
Γ	–	Threshold as a percentage of input matrix size.
g	–	PNS rheobase $(\mathrm{V} \cdot \mathrm{m}^{-1})$.
G_f	–	Frequency encoding gradient strength $(\mathrm{T} \cdot \mathrm{m}^{-1})$.
h	–	Imaging slice thickness (mm).
I	–	Voxel signal intensity.
Δk	–	k-space resolution (m^{-1}).
k	–	Spatial frequency coordinate of k-space (m^{-1}).
λ	–	Eigenvalue.
μ_e	–	External magnetic permeability $(\mathrm{H} \cdot \mathrm{m}^{-1})$.
μ_i	–	Internal magnetic permeability $(\mathrm{H} \cdot \mathrm{m}^{-1})$.
m	–	Number of observations after thresholding.
M_0	–	Equilibrium longitudinal magnetization $(\mathrm{A} \cdot \mathrm{m}^{-1})$.
n	–	Number of input observations.
N	–	Operator sample size.
N_a	–	Number of signal averages.

N_y	–	Number of steps in the first direction of phase encoding.
N_z	–	Number of steps in the second direction of phase encoding.
Ω	–	Gradient ramp duration (ms).
O	–	Order of computational complexity.
$\Delta\phi$	–	RF pulse phase cycling (°).
ϕ	–	Signal phase shift (°).
Φ	–	Contact angle of intersection between slice volumes in a multi-slice acquisition (°).
ψ	–	Contribution of an observation to a principal component.
p	–	Dimensionality of PCA observations.
$\mathbf{Q}$	–	Matrix of observations offset by weighted mean.
ρ	–	Proton density.
$\mathbf{r}$	–	Observation.
$\mathbf{R}$	–	Matrix of observations .
$\bar{\mathbf{s}}$	–	Weighted centroid of observations.
$\mathbf{s}$	–	Weighted observation.
$\mathbf{S}$	–	Weighted observation matrix.
S	–	k-space signal acquisition.
τ	–	Image frame duration (ms).
θ	–	Localization angular error between needle and slice orientation (°).
T_1	–	Longitudinal magnetization relaxation time constant (ms).
T_2	–	Transverse magnetization relaxation time constant (ms).
T_a	–	Acquisition time (ms).
T_c	–	Time required for a complete interleaved scanning cyle (ms).
T_E	–	Echo time (ms).
T_m	–	Time required for a manual scan plane alignment (ms).
T_R	–	Repetition time (ms).
T_s	–	Time required for active shimming calibration (ms).
$\hat{\mathbf{u}}$	–	Eigenvector.
ΔV	–	Voxel volume (mm^3).
w	–	Weighting factor.
"$x'y'z'$"	–	Distorted Cartesian image coordinates (mm).

List of Abbreviations

2D	–	Two Dimensional.
3D	–	Three Dimensional.

API	–	Application Programming Interface.
bSSFP	–	balanced Steady State Free Precession.
CORBA	–	Common Object Request Broker Architecture.
CPU	–	Central Processing Unit.
CT	–	Computed Tomography.
DICOM	–	Digital Imaging and Communications in Medicine.
EPI	–	Echo Planar Imaging.
ETL	–	Echo Train Length.
FOV	–	Field of View.
GUI	–	Graphical User Interface.
ICNIRP	–	International Comission on Non-Ionizing Radiation Protection.
IEC	–	International Electrotechnical Commission.
IFE	–	Siemens Interactive Front End.
MCU	–	Microcontroller Unit.
(MRg)HIFU	–	(MR-guided) High Intensity Focused Ultrasound.
MRI	–	Magnetic Resonance Imaging.
NRR	–	Noise Reduction Ratio.
PC	–	Personal Computer.
PCA	–	Principal Component Analysis.
PNS	–	Peripheral Nerve Stimulation.
RAM	–	Random Access Memory.
RF	–	Radiofrequency.
ROI	–	Region of Interest.
SAR	–	Specific Absorption Rate.
SNR	–	Signal to Noise Ratio.
TSE	–	Turbo Spin Echo.
VU	–	Volume Unit.
XTC	–	eXTernal Control protocol.

Chapter 1

Introduction

1.1   MRI-guided Interventions

Intra-operative image guidance provides a means of verifying treatment and device placement during interventional procedures [1]. Localization of needles or cannulas with respect to target regions or critical anatomy is required during procedures of the brain, breast, prostate, liver or musculoskeletal system such as biopsies or radiation therapy [2]. Endovascular procedures such as angioplasty require tracking of catheters, guidewires and stents. Thermal therapies such as high intensity focused ultrasound (HIFU), cryoablation, and radiofrequency, microwave or laser ablation involve precise placement of probes, transducers and subsequent thermometry measurement to monitor thermal dosage [3, 4, 5, 6, 7]. Real-time imaging methods are advantageous for visualizing these procedures because they can account for target motion or displacement of the surrounding tissue during treatment or device placement. MRI-guided interventions in closed bore MRI scanners can be performed with freehand device placement methods that are conducted in real time during rapid image acquisition [8]. Intraoperative targeting of brain regions or other organs can be performed using real-time MR-guided prospective stereotaxy [9]. MRI guidance is a desirable choice among imaging modalities due to real-time capabilities of certain pulse sequences, potentially improved soft tissue contrast compared to computed tomography (CT) or ultrasound, multi-planar imaging capabilities, and the lack of ionizing radiation [1, 10]. Technical challenges arise from working within the environment of the MRI scanner suite such as the requirement for non-ferromagnetic instrumentation, restricted patient access and distraction to clinicians from various occupational exposure effects such as peripheral nerve stimulation

(PNS), absorption of radiofrequency energy and high sound pressure levels [11, 12].

1.2 Motivation

This thesis investigates the accuracy of a new image-based localization technique and the feasibility of its implementation for real-time MR scan plane alignment to explore this technique as an alternative to existing methods. Without hardware or software modification, communication-prohibitive sound pressure levels interfere with the general MR-guided interventional workflow shown in Fig. 1.1. Real-time dynamic imaging during device placement can take the form of fixed scan planes aligned with an immobilized region of interest and planned device trajectory [1] or iteratively stopping and starting the scanner for manual scan plane realignment [13, 14]. While a scanner has been stopped, manual alignment of scan planes requires a clinician to either leave the scan room to adjust scan plane geometry directly or provide blind guidance to a technician via intercom or headset. A single iteration of this process can take several minutes including execution of required scout imaging sequences and shimming calibration. Device placement and/or treatment may progress only when a device, target region and visualization scan planes are all properly aligned. In practice, there has been limited use of automated interventional systems which localize and track devices within an MR environment based on optical fiducial markings, MR-visible patterns, RF tracking coils or fiber optic components [15]. Use of these systems is hindered by the crowded environment around a patient during an intervention and requires expensive, time consuming modifications to the scanner hardware and MR-compatible instrumentation which may pose additional safety risks.

1.3 Thesis Scope and Objectives

The objective of this work is to develop an MR image-based device localization mechanism for linearly shaped interventional device which meets the following criteria:

1. Based on passive methods i.e. requires no modification to interventional instrumentation

2. Achieves sufficient accuracy for visualization scan plane alignment

3. Technically feasible to implement along with real-time imaging on an MR scanner

4. Engaged with hands-free operation
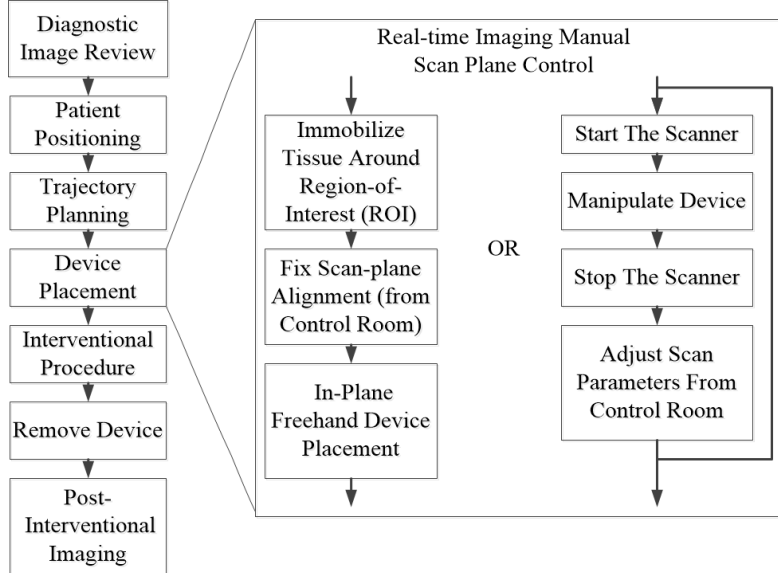
Figure 1.1: General MRI-guided intervention visualization workflow without hardware or software modification.

To realize these objectives, relevant background information is first presented in Chapter 2 to provide the reader with an understanding of pertinent topics in MR image guidance and technical considerations there-of. This background is followed by a literature review in Chapter 3 which describes recent work in the area of real-time imaging platforms, imaged-based localization techniques, and automated scan plane alignment. Chapter 4 sets out the main thesis work describing two experiments to assess first the preliminary effectiveness of a proposed localization algorithm and secondly the feasibility of the algorithms incorporation into device tracking system for MR scanners. Chapter 5 presents results collected from phantom and *ex-vivo* trails. §5.1 and §5.2 presents results for the effectiveness and feasibility experiments respectively. Chapter 6 explores the required parameters and accuracy of the localization algorithm, time trial results from the interleaved scanning experiments along with practical considerations for use of the overall mechanism. Example figures are provided to illustrate situations in which these considerations are relevant. Conclusions about the achievements of this work along with recommendations for its potential applications are discussed in Chapter 7.

Chapter 2

Background

Pertinent background information is presented in this chapter to provide the reader with a precursory understanding of topics in MR image guidance. These topics include passive device localization and visualization, rapid imaging sequences, noise and artifacts observed in these images, as well as occupational exposure effects. Where possible, example images and mathematical descriptions are provided to give both qualitative and quantitative explanations.

2.1 MR Signal and Localization

For the sake of brevity, only a minimal explanation of MRI signal acquisition is provided and additional information can be found in numerous introductory resources [16, 17, 18]. In the MR-imaging process, nuclear spins (typically hydrogen nuclei) within subject tissue precess about an externally applied static magnetic field axis and are targeted with a Radiofrequency (RF) perturbation. The spins are subsequently spatially encoded according to the superposition of applied magnetic field gradients. The net magnetization $\mathbf{M}$ of each encoded volume element (voxel) contains a longitudinal component $\mathbf{M}_{\shortparallel}$ parallel to the static magnetic field, and an orthogonal transverse component $\mathbf{M}_{\perp}$ which induces a signal measured after a selected echo time interval T_E. The process is repeated at intervals of a selected repetition time T_R as required to populate a matrix spatial frequency measurements (k-space) which forms a reciprocal domain to the complex image space where magnitude and phase information is reconstructed graphically by means of inverse Fourier transform. The processes by which $\mathbf{M}_{\perp}$ and $\mathbf{M}_{\shortparallel}$ relax after perturbation into their original state are independent and occur according to respective magnetization recovery time constants T_1 and T_2 which are properties of the tissues from which signal is collected.
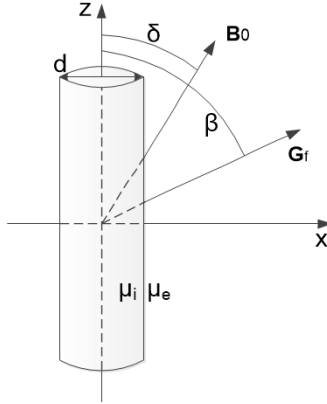
Figure 2.1: Model of interventional instrument passive visualization.

A main feature of MR-imaging is that contrast is established between tissues by selecting imaging parameters such as T_E, T_R and RF excitation flip angle α according to T_1 and T_2 as well as an additional tissue property, proton density ρ. This work deals primarily with gradient recalled echo (GRE) images which do not employ the 180° re-focusing pulses characteristic of spin echo (SE) sequences. For gradient echo imaging of tissues where transverse magnetization is effectively spoiled between T_R periods, a steady-state voxel signal intensity I_{ss} arises during the imaging process according to the following relation:

$$I_{ss} \propto \frac{\rho \sin\left(\alpha\right)\left(1 - E_1\right)}{1 - \cos\left(\alpha\right)E_1} E_2^* \tag{2.1}$$

where α is RF excitation angle, $E_1 = \exp\left(-T_R/T_1\right)$ and $E_2^* = \exp\left(-T_E/T_2^*\right)$. T_2^* is the effective time constant for relaxation of traverse magnetization accounting for both the time constant of decay from natural interaction of nuclear spins (T_2), as well as the contribution resulting from average field inhomogeneity across the voxel ΔB [16] which for gradient echo images is given by:

$$\frac{1}{T_2^*} = \frac{1}{T_2} + \gamma|\Delta B| \tag{2.2}$$

2.2 Model for Passive visualization of Device Artifacts

A simple model for passive visualization of interventional instruments given by Ladd *et al.* [19]. is illustrated in Fig. 2.1 as a long cylindrical element of diameter d, positioned at an angle δ from the main static magnetic field $\mathbf{B_0}$ and at an angle β from the frequency encoding gradient $\mathbf{G_f}$. Spatial distortion and signal dephasing result from differences between the element's internal magnetic permeability μ_i and the permeability of the surrounding tissue μ_e. The following

equations give spatially distorted image coordinates (x', y', z') as a function of right-handed object coordinates (x, y, z),[1] frequency and slice-selection gradient strengths G_f and G_s, as well as magnetic field intensity shift ΔB:

$$x' = x + \frac{\Delta B}{G_f} \cos \beta \tag{2.3}$$

$$y' = y + \frac{\Delta B}{G_s} \tag{2.4}$$

$$z' = z + \frac{\Delta B}{G_f} \sin \beta \tag{2.5}$$

$$\Delta B = -B_0 \left(\frac{d}{2}\right)^2 \left(\frac{\mu_i - \mu_e}{\mu_i + \mu_e}\right) \left(\frac{x^2 - y^2}{(x^2 + y^2)^2}\right) \sin^2 \delta \tag{2.6}$$

which for gradient echo images, relates to voxel signal intensity I to needle angle δ according to Eq. 2.1 by:

$$I(x, y, \delta) \propto \exp\left(-\kappa(x, y) \sin^2 \delta\right) \tag{2.7}$$

where

$$\kappa(x, y) = T_E \gamma B_0 \left(\frac{d}{2}\right)^2 \left|\left(\frac{\mu_i - \mu_e}{\mu_i + \mu_e}\right) \left(\frac{x^2 - y^2}{(x^2 + y^2)^2}\right)\right| \geq 0 \tag{2.8}$$

Three characteristics are observed from this model and are exhibited in Fig. 2.2:

- The device element itself generates no signal.

- Even when surrounded by homogeneous tissue, spatial distortion will create asymmetrical signal pile-up about the device axis as a function of the needles angle from the main magnetic field δ as well as needle angle from the frequency encoding gradient β.

- Magnetic field inhomogeneity will contribute to signal dephasing in the vicinity of the element as the result of increased T_2^* effects, also a function of δ. This dephasing is radially symmetrical about the needle axis.

Scan parameters for Fig. 2.2 are shown in Table 2.1.

An interventional radiologist must be familiar with these characteristics when performing procedures under MRI guidance with non-ferromagnetic instrumentation and it is critical from

---

[1]Here, x, y and z directions apply only to the device orientation and are distinct from Cartesian coordinate systems used elsewhere in this work.
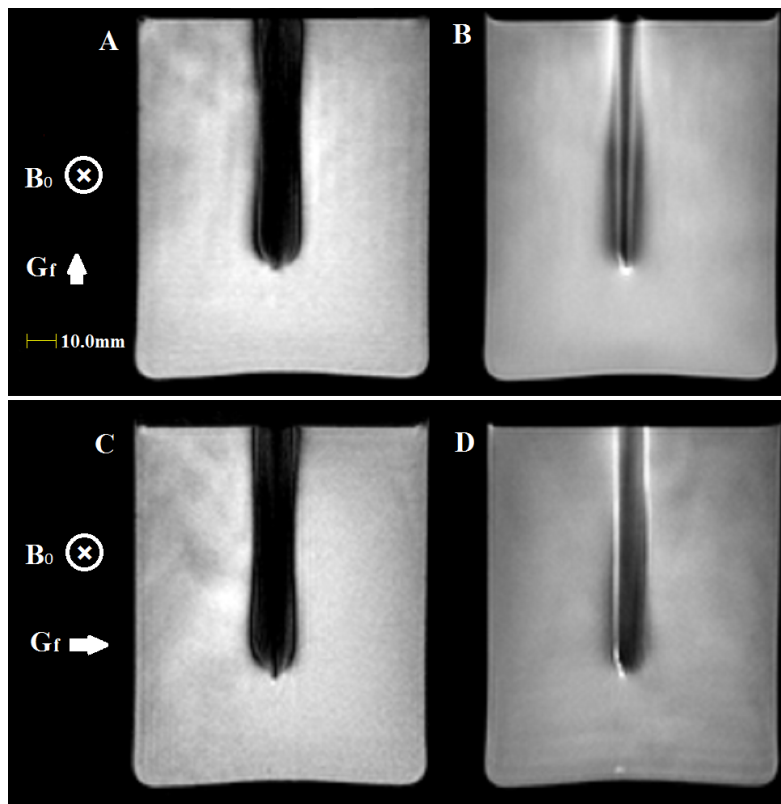
Figure 2.2: Artifacts generated from a 4 mm diameter biopsy needle in water.

Table 2.1: Parameters selected for scans depicted in Fig. 2.2.

Scan	A	B	C	D
TR	3000 ms	3000 ms	3000 ms	3000ms
TE	3 ms	12 ms	3 ms	12 ms
Flip angle	70°	90°	70°	90°
Slice thickness	10 mm	10 mm	10 mm	10mm
FOV	150×150 mm^2	150×150 mm^2	150×150 mm^2	150×150 mm^2
Acquisition matrix	152×150	152×150	152×150	152×150
Reconstruction matrix	160×160	160×160	160×160	160×160
N_a	1	1	1	2

them to see a projection of the entire artifact within a dynamic image. From an image processing point of view, an interventional device's susceptibility artifact appears in gradient echo images mainly as a null region emanating along the device's position. As per the equations above, the size and intensity of this region depends on the difference of susceptibility of a device from surrounding tissue, device radius, the strength and orientation relative to the device of static magnetic field and gradient fields. Fig. 2.2 also shows a characteristic 'bloom' of distortion and signal dephasing around the needle tip locations not described by Eqs. 2.3 - 2.1. The exact distribution of these blooms depend on instrument tip geometry and can be modeled by superposition of induced elementary dipole fields as simulated numerically by Muller *et al.* [20]. Appearance of the bloom is most pronounced at the actual tip location and can be minimized when the needle is oriented anti-parallel to the scanner frequency encoding gradient direction but also parallel to the scanner static magnetic field orientation [21].

To contain the signal void of a biopsy needle entirely within a limited region of interest across a slice volume, localization error (position and angle) between the needle and slice must be contained within limits determined according to the geometry of Fig. 2.3. This illustration of the worst case needle orientation is used to determine the following condition for total biopsy needle containment within a rectangular slice:

$$h - \frac{d}{\cos \theta} \geq |2\epsilon + \text{ROI} \cdot \tan \theta| \qquad (2.9)$$
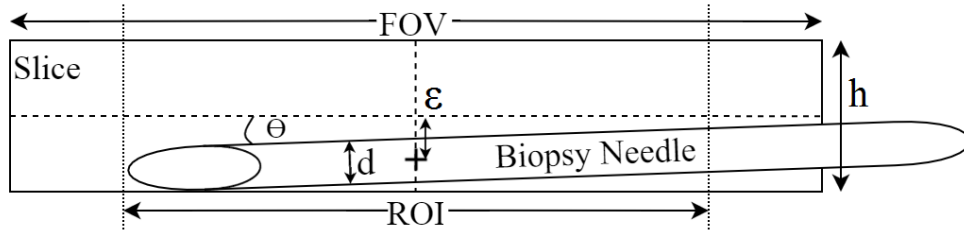
Figure 2.3: A cross-sectional diagram illustrates the relevant parameters in determining minimum localization accuracy required to contain a biopsy needle within a region of interest across a visualization slice volume.

where h is slice thickness, ROI (region of interest) is the length of the slice field of view (FOV) over which the needle is to be contained, d is biopsy needle outer diameter, ϵ is needle centroid localization error along the slice select direction and θ is angular localization error within the plane illustrated by the figure.

2.3 Signal to Noise Ratio

Much of this work pertains to calculation of optimal scan plane alignment based on image data containing noise with a broad spatial distribution. For the remainder of Chapter 2, x, y and z directions refer to frequency encoding, phase encoding, and slice-selection dimensions in a right-handed coordinate system aligned with slice geometry as shown in Fig. 2.4. These directions are linear combinations of foot-head, right-left and anterior-posterior patient axes with corresponding 'F-H', 'R-L' and 'A-P' designations. Each MRI scan is composed from voxels (volume elements) with associated signal magnitude and phase information. The signal amplitudes of scan voxels can be represented by pixels of MRI magnitude image data, with each pixel containing noise with an approximately Gaussian distribution resulting from receive coil resistance and inductive tissue losses [22]. In terms of scan parameters, MR image SNR is generally proportional to voxel volume ΔV and the square root of acquisition time T_a [23]:

$$SNR \propto \Delta V \sqrt{T_a} \tag{2.10}$$

and

$$T_a = T_R \times N_y \times N_z \times N_a \tag{2.11}$$
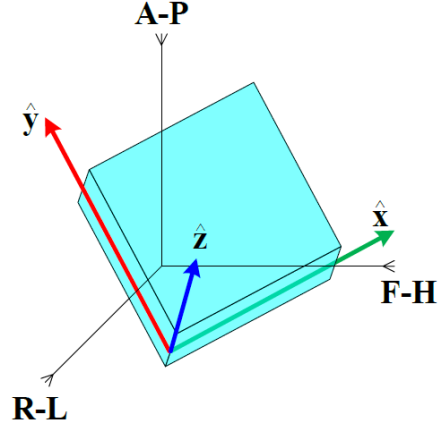
Figure 2.4: Illustrations of coordinate system vectors that define the geometry of a given imaging volume.

where N_y and N_z are the number of phase encoding steps in the phase encoding and slice-selection directions of the scan respectively [24].[2] N_a is the number of signal averages performed.

2.4 Structured Noise

In addition to the noise inherent to each voxel, different phenomena that occur during acquisition of MRI scans exhibit patterned interference across the MR image space. The spatial distribution of this noise is discussed in the following subsections and with included mathematical descriptions.

2.4.1 Motion Artifacts

Subsequent discussion in this work regarding orientation ('scout') scan acquisition is related to correction of artifacts contained within data constructed from these scans. Optimal scan plane alignment can be calculated from the element-wise subtraction of two three-dimensional (3D) localizer data sets.[3] 3D MRI acquisitions employ an additional dimension of spatial encoding, namely a second application of phase encoding in the slice-selection direction of the scan volume. A 3D EPI scan acquisition time can take from several seconds to several minutes according to Eq. 2.11. The portion of each T_R required for signal sampling is negligible in comparison to the time period over which significant subject motion will take place inside the scanner. However, as many phase encoding steps are required for this sequence as the number of voxel elements

---

[2]$N_z = 1$ for the case of a 2D slice projection image.

[3]In this work, the term 'scan' will be distinguished from 'image' or 'data set' by the inverse Fourier transform reconstruction of signals acquired during a scanning sequence.

along respective phase encoding directions. Even the shortest repetition times, on the order of single milliseconds, require a total scan duration of several seconds over which significant subject motion may occur, particularly periodic patient motion due to the involuntary nature of the cardiac or respiratory cycle. Hedley *et al.* [25] describe a two-dimensional case of translation of voxel signal intensity I during acquisition of signal S which is extended to three dimensions as:

$$I = I(x - p, y - q, z - r) \tag{2.12}$$

$$S = S(k_x, k_y, k_z) = \int \int I(x, y, z) \exp\left(-i2\pi(k_x x + k_y y + k_z)\right) dx\,dy\,dz \tag{2.13}$$

where x, y, z are the spatial coordinates of an image space, and p, q, r are a rigid translation offset. k_x, k_y, k_z are spatial frequency coordinates. For the blipped-gradient or Cartesian k-space trajectories used in this work, rows of k-space along phase encoding directions are acquired over greater lengths of time than individual samples during frequency encoding readout. The result is a higher likelihood that voxel signal amplitudes could be modulated due to motion between phase encoding steps. $p, q, r = p(k_y, k_z), q(k_y, k_z), r(k_y, k_z)$ are thus assumed to depend only on k_y and k_z phase encoding spatial frequency coordinates. A signal $\hat{S}$ acquired during translation of tissue will encounter a non-uniform phase shift ϕ:

$$\hat{S}(k_x, k_y, k_z) = \exp\left(-i\phi(k_x, k_y, k_z)\right) S(k_x, k_y, k_z) \tag{2.14}$$

$$\phi(k_x, k_y, k_z) = 2\pi \left[k_x p(k_y, k_z) + k_y q(k_y, k_z) + k_z r(k_y, k_z) \right] \tag{2.15}$$

By property of the Fourier transform relationship between k-space and image space, the resulting image exhibits motion artifact where ripples of the affected tissue are apparent everywhere the across phase encoding directions of the reconstructed data set as shown in Fig. 2.5.

2.4.2 Aliasing

As noted, the Fourier transform relates signal space (k-space) and image space. A consequence of the discretization of k-space is spatial periodicity across image space resulting in possible aliased voxel signal intensity I_a extended to three dimensions from the properties of the inverse discrete Fourier transform [26]:

$$I_a(x, y, z) = I(x, y, z) + I\left(x + \frac{n}{\Delta k_x}, y + \frac{m}{\Delta k_y}, z + \frac{l}{\Delta k_z}\right), \forall (n, m, l) \in \mathbb{Z}^3, \tag{2.16}$$

where k-space sample spacing Δk is reciprocal to field of view in x, y and z directions denoted as subscripts. If subject size exceeds field of view for a given dimension of a scan, the subject image

Figure 2.5: Left: A biopsy needle artifact generated within a porcine muscle sample. Right: Motion of the needle during acquisition creates a motion artifact along the entire phase encoding direction (vertical).

will begin to 'wrap around' on itself creating the well known aliasing artifact shown in Fig. 2.6. The varying phase of aliased voxels causes signals to combine constructively in some portions of the image as well destructively in others. Aliasing artifact can be mitigated in the frequency direction by means of oversampling during signal measurement with the scanner receiver system analog-to-digital converter, effectively widening the image FOV in this direction without time penalty. To oversample in any phase encoding direction incurs a time penalty according to Eq. 2.11. Compensatory techniques can be employed to keep acquisition time constant such as reducing the number of signal averages or increasing voxel size along the aliased direction in proportion to a larger FOV.

2.4.3 Cross-talk Artifacts

During a $2D$ multi-slice acquisition, intersecting or adjacent slices are excited in succession. If signal within a slice volume is repeatedly attenuated by prior RF excitation from a preceding slice in the sequence, the resulting image artifact is referred to as 'cross-talk'[16] and shown in Fig. 2.7. The width of cross-talk bands are given by the projection of an intersecting slice of thickness h at contact angle Φ is calculated from RF excitation pulse bandwidth BW_{RF}, tissue gyromagnetic ratio γ and slice-selection gradient strength G_s is given by:

$$\frac{h}{\sin \Phi} = \frac{BW_{RF}}{\gamma G_s \sin \Phi}. \tag{2.17}$$
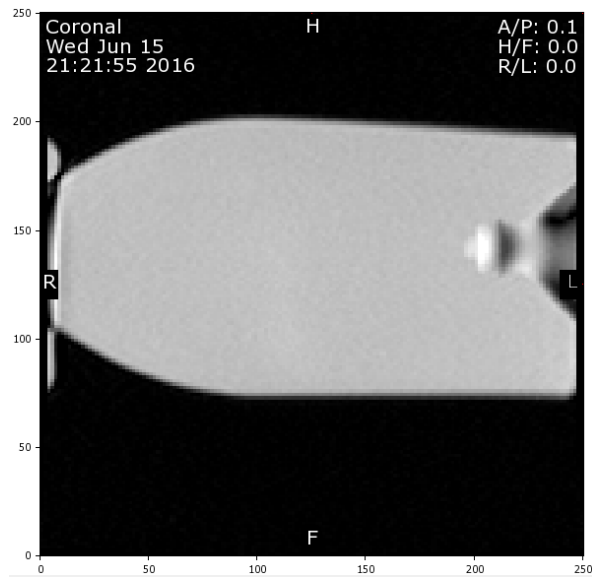
Figure 2.6: A phantom subject size exceeds the scan FOV in the phase encoding direction of this 2D acquisition resulting in aliasing artifact.
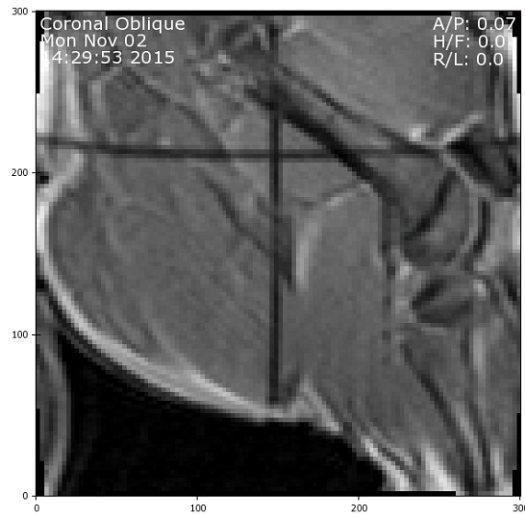
Figure 2.7: An image shows stark 'cross-talk' artifacts corresponding to the locations of orthogonally intersecting slices.

2.5 Fast Imaging Sequences for Real-time MRI

MR-guided interventional procedures require fast imaging sequences to provide real-time information to a clinician about placement of a device relative to a target position. Common choices for this requirement include Echo Planar Imaging (EPI), balanced Steady State Free Precession (bSSFP)[4], and Turbo Spin Echo (TSE) Sequences [1, 27, 28]. Appropriate choices are desired for the experiments described in Chapter 4. The following case set of parameters for real-time interactive multi-slice visualization of needle placement based on Rothgang *et al.*(2013) [29] serve as a basis for making a comparison between commonly used fast imaging sequences for interventions: shortest T_R, shortest T_E, $\alpha = 20°$, slice thickness = 10 mm, FOV = 300×300 mm^2, acquisition matrix = 192×192. A primary criterion for selecting a sequence is the simply the time required per image frame acquisition. The shorter the amount of time required to acquire an image frame, the higher the value of effective 'frame rate' of displayed images and the shorter the amount of time experienced as latency by a clinician operator in obtaining visual feedback about the placement of a device. Generally, video-based interactive manual activities require a lag time of less than 300 ms to maintain immersive effect [30] while longer delays will degrade an operators natural association between their manual actions and corresponding visualization. Fig. 2.8 shows the time the required for the Philips Achieva 3.0 T scanner to obtain one image frame using respective fast imaging sequences (a) EPI and bSSFP and (b) TSE at various echo train lengths (ETL).[5] The lag requirement of 300 ms is marked with a dashed line in both cases. The graph indicates that with sufficient echo train lengths, EPI and bSSFP based images can be collected from the Philips Achieva 3.0 T at rate even faster than that required to maintain immersive clinician interaction. Additional time savings can be achieved through 'half-scan' acquisition where due to the conjugate symmetry of k-space, coverage of a blipped gradient or Cartesian trajectory can be limited to slightly more than half of k-space and the remaining rows populated by interpolation [17] as illustrated in Fig. 2.9. Acquisition time T_a within Eq. 2.11 is reduced accordingly along with image signal to noise ratio (SNR) according to Eq. 2.10. Half-scans are implemented in Philips MR Imaging as an option for all sequences used in §4.2 and their application will be discussed in Chapter 4. An additional consideration in interpreting Fig.

---

[4]bSSFP is implemented in Philips MR Imaging release 3.2.3 as a contrast enhancement compatible with gradient echo imaging sequences such as EPI.

[5]An ETL of one indicates that no fast imaging is used i.e. one RF excitation is applied per phase encoding step.
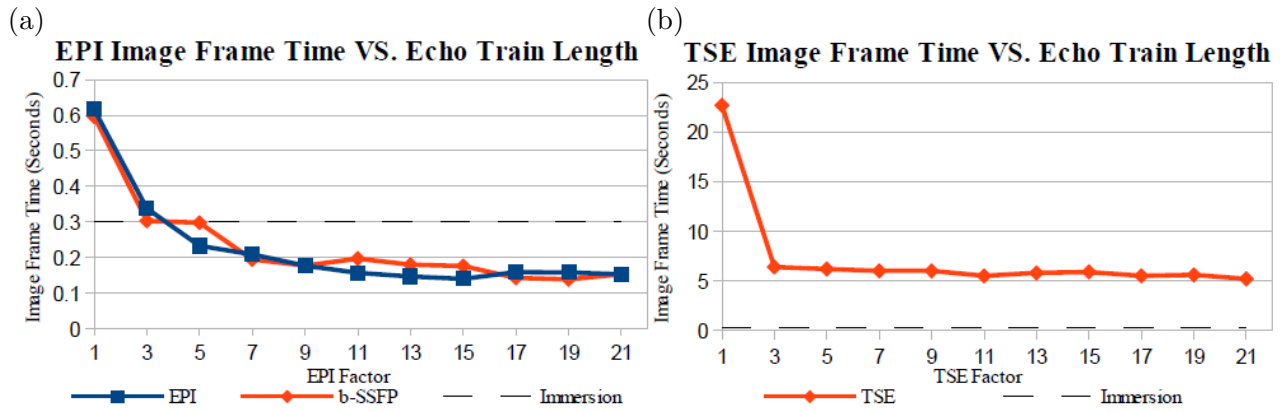
Figure 2.8: A comparison of fast imaging pulse sequence image frame times.
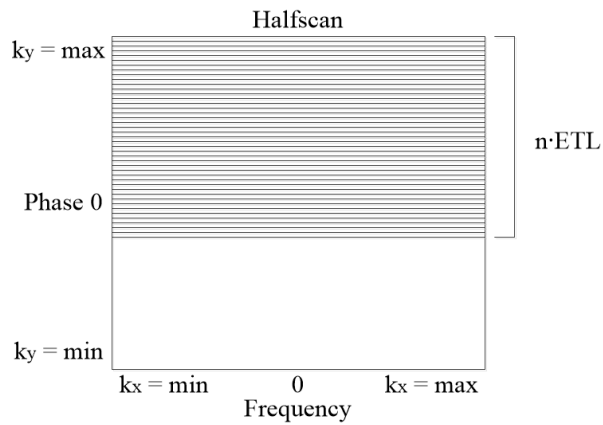
Figure 2.9: Illustration of 'half-scan' k-space acquisition.
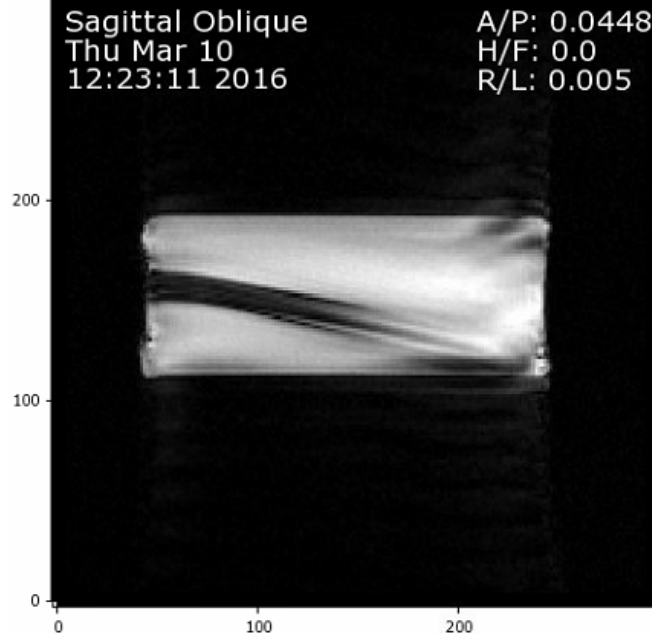
Figure 2.10: A phantom affected by geometric distortion characteristic of EPI imaging with a long ETL.

2.8 (a) is that geometric distortion and loss of SNR increase with echo train length. The basic principal is that when echo train duration is increased, additional localization error and signal dephasing from field inhomogeneity will accrue. Signal localization will be shifted in frequency and phase encode directions according the following expression:

$$(x', y', z') = \left(x + \frac{\Delta f(x,y,z)}{BW_f} \text{FOV}_x, \ y + \frac{\Delta f(x,y,z)}{BW_{py}} \text{FOV}_y, \ z + \frac{\Delta f(x,y,z)}{BW_{pz}} \text{FOV}_z \right) \qquad (2.18)$$

where x', y', z' are distorted image coordinates, x, y, z are the corresponding object coordinates across field of view FOV and $\Delta f = \gamma \Delta B$ is precession frequency shift resulting from field inhomogeneity. BW_f, BW_{py} and BW_{pz} are frequency and phase encoding signal bandwidths which are reciprocal to sampling time and total readout time respectively. BW_{py} and BW_{pz} increase directly with ETL during EPI-based sequences and because $BW_f \gg BW_{py} > BW_{pz}$ in this case, spatial distortion appears mostly along the phase encoding directions. Fig. 2.10 depicts geometric distortion occurring in an EPI image with ETL = 11 of a phantom where the central signal void created with an air-filled tube inserted into a cylindrical water bottle should appear straight and diagonal.

T_a is also reduced in proportion to ETL and consequently so is SNR according to Eq. 2.10. In addition to these image defects, images acquired with bSSFP sequences suffer from
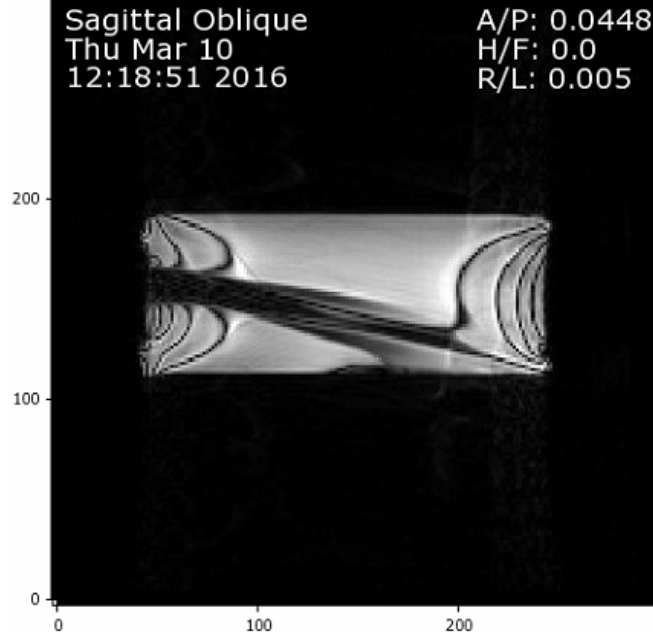
Figure 2.11: A phantom affected by dark banding characteristic of bSSFP imaging and geometric distortion characteristic of a long ETL.

'dark banding' artifacts as shown in Fig. 2.11. Like Fig. 2.10, Fig. 2.11 also depicts geometric distortion with $ETL = 11$ occurring in the same phantom.

Dark bands correspond to locations in the image which coincide with transition bands of the bSSFP transverse magnetization profile [31] shown in Fig. 2.12.[6] The following expressions show signal magnitude I_{bssfp} for balanced SSFP is be expressed a function of phase shift ϕ of spins accumulated in the T_E period after RF excitation:

$$I_{bssfp} \propto M_0 \frac{(1 - E_1) \cdot \sin\alpha \cdot \sqrt{(E_2 \sin\phi)^2 + (1 - E_2 \cos\phi)^2}}{(1 - E_1 \cos\alpha) \cdot (1 - E_2 \cos\phi) - E_2 \cdot (E_1 - \cos\alpha) \cdot (E_2 - \cos\phi)} \tag{2.19}$$

where M_0 is equilibrium longitudinal magnetization, α is RF excitation flip angle and $E_{1,2} = \exp(-TR/T_{1,2})$. ϕ is related to magnetic field inhomogeneity ΔB by the following expression:

$$\phi = \gamma T_E \Delta B. \tag{2.20}$$

Inhomogeneity is an inherent part of an interventional device susceptibility artifact as presented in §2.2 and consequently repositioning of a device like that represented in Fig. 2.11 alters the dis-

---

[6]Fig. 2.12 is calculated from $T_1 = T_2 = 3000$ ms, $T_R = 5$ ms, $\alpha = 70°$ and shifted according to RF pulse phase cycling $\Delta\phi = 180°$ [31, 32].
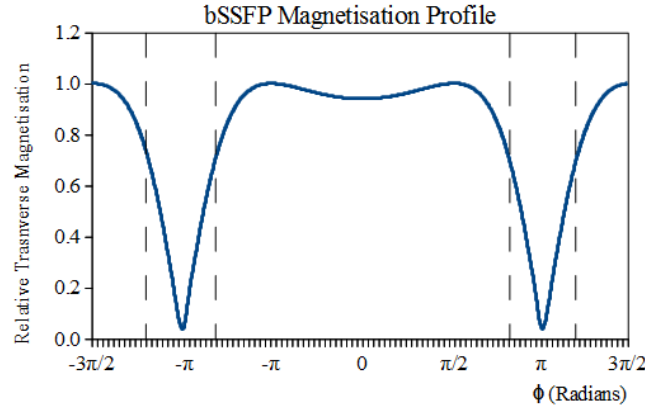
Figure 2.12: A transverse magnetization profile of bSSFP. Attenuated 'transition bands' are shown with a dashed line.

tribution of dark banding across image space, interfering with artifact segmentation techniques. It is worth noting a dependency on both longitudinal and transverse magnetization recovery time constants T_1 and T_2. This 'mixed contrast' property of bSSFP images is at odds with achieving independently 'T_1 weighted' or 'T_2 weighted' contrast within images, control of which is desirable for device localization and tumor visualization respectively [1, 27]. Fig. 2.8 shows unacceptable image frame times for a TSE sequence in terms of real-time imaging, however the resulting images show relevant image quality characteristics as can be observed in Fig. 2.13 obtained with an $ETL = 11$. The spin echoes induced in this sequence with successive 180° RF pulses between phase encoding steps between readouts to reverse signal dephasing resulting from static magnetic field inhomogeneity. This periodic inversion effectively rewinds and replays phase dispersion of nuclear spins within a voxel to recoup accrual of phase-encoded localization error throughout long echo trains, thus protecting images from the significant spatial distortion seen in the EPI-based images [33]. Conveniently, all pulse sequence types discussed in this section are available within Philips MR in 3D scan modes. These implementations execute a second order of phase encoding to distinguish contiguous voxels along the slice-selection direction [33, 17]. 3D acquisitions will be employed in Chapter 4 as 'orientation scans' from which device position and alignment will be determined automatically, as well as placement verification scans. Based on the limitations discussed in this section, gradient echo-techniques *without* EPI or bSSFP can provide both the imaging speed and resilience to geometric distortion required to be employed for orientation and
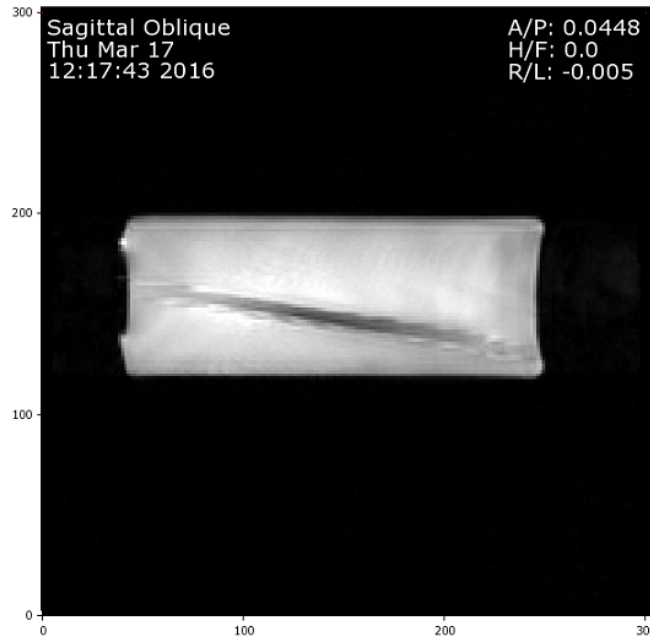
Figure 2.13: A phantom exhibits improved image quality with use of a TSE sequence.

visualization scan imaging.

2.6 Occupational Exposure

Occupational exposure effects of MR scanner use pose potential hazards to clinicians or patients during an intervention. For example, vertigo can result from fast head movements near the opening of a scanner bore. A static magnetic field strength of 0.5 T shifted by $\frac{\partial B}{\partial t} = 0.7 \, \text{T} \cdot \text{s}^{-1}$ can induce an experience of vertigo on par with a blood alcohol concentration of 0.09% [34]. Other effects relevant considered in this work are described in the following subsections.

2.6.1 Peripheral Nerve Stimulation

Rapidly switching gradient magnetic fields applied during imaging can induce stimulation of peripheral nerves in an imaging subject or in those standing in close proximity to the gradient coils [35, 1]. Gradient fields reach their highest amplitudes at the end of the maximal field of view. When gradients are pulsed periodically during an imaging sequence, currents may be induced in nearby neural tissue potentially resulting in twitching and contraction of muscles. This phenomena is not dangerous in itself but presents a warning of vital nerve stimulation and may interfere with motor control. GRE imaging can induce $1.6 \, \text{T} \cdot \text{s}^{-1}$ at the entrance of an Philips Achieva 3.0 T scanner bore vs $0.22 \, \text{T} \cdot \text{s}^{-1}$ corresponding International Commission on

Non-Ionizing Radiation Protection (ICNIRP) guideline [36]. Limits on rate of change of the gradient coil magnetic flux density with time $\frac{dB}{dt}$ are defined by the International Electrotechnical Commission (IEC) Medical Electrical Equipment Standard 60601-2-33 [37] as a percentage of median PNS detection threshold at which 50% of the population is expected to perceive stimulation effects. This median threshold is modeled in hyperbolic form from empirical data in the following equation:

$$\frac{dB}{dt} < g\left(1 + \frac{c}{\Omega}\right) \tag{2.21}$$

where $g = 20$ T $\cdot$ s^{-1} is the standard rheobase i.e. the mean $\frac{dB}{dt}$ stimulation threshold for an infinite pulse duration, $c = 0.36$ ms is the standard chronaxie and gradient ramp duration at which the stimulation threshold is twice the rheobase and Ω is the stimulus duration in milliseconds. *Normal operating controlled mode* limits $\frac{dB}{dt}$ within 80% of the median threshold. *first level controlled operating mode* requires a warning prompt for scans operating between 80 % and 100 % of the median threshold. The Philips Achieva 3.0 T is not permitted to run in *Second Level Controlled Operating Mode* which allows operation above 100 %. Additional IEC limits are imposed to prevent cardiac stimulation according to the following threshold:

$$\frac{dB}{dt} < \frac{g}{\left[1 - \exp\left(-\frac{\Omega}{3 \text{ ms}}\right)\right]} \tag{2.22}$$

Peripheral Nerve Stimulation is an important consideration for assessing the feasibility of scanner control techniques which involve the rapidly interleaved scan protocols because of the potential risks posed to patient and clinician.

2.6.2 Specific Absorption Rate

During a scan acquisition, RF pulses are applied to subject located in the scanner to perturb nuclear spins in such a manner that they will emit measurable signal. Some of this RF energy is absorbed by the subject tissue and dissipated as heat resulting in potentially harmful effects. This absorption is monitored in terms specific absorption rate (SAR) measured in units of W $\cdot$ kg^{-1}. Limits on SAR exposure are defined by the International Electrotechnical Commission (IEC) Medical Electrical Equipment Standard 60601-2-33 [37] and summarized in Table 2.2. Gradient echo based sequences minimize SAR by eliminating 180° refocusing pulses used in spin-echo based techniques and by use of flip-angle reductions [38]. An insulated slab of tissue would experience a temperature rise of about 1° C per hour under SAR conditions of 1 W $\cdot$ kg^{-1} [39].

SAR level	Body W·kg^{-1}		Local W·kg^{-1}			Comment
	Whole	Partial	Head	Torso	Extremities	
Level 0	≤2	2-10	3.2	10	10	Normal operating mode
Level 1	≤4	4-10	3.2	20	20	Requires user confirmation
Level 2	>4	>(4-10)	>3.2	>10	>20	Not used in clinical routine

IEC values are taken as average over six minutes. Partial body values refer to the ratio of exposed mass over patient mass.

Table 2.2: Specific absorption rate limits as defined by International Electrotechnical Commission (IEC) 60601-2-33

SAR estimates provided by the Philips Achieva 3.0 T are calculated from a proprietary model and are independent of subject size. They appear to consistently overestimate actual SAR as a worst-case estimate [40]. The SAR figures collected during the experiments described in Chapter 4 provide assurance that patients directly exposed to RF excitation from the body coil or clinicians working in close proximity to this coil would be exposed to a SAR level *less than or equal to* the levels reported by the scanner.

2.6.3   Noise Exposure

The construction of MRI scanners can be compared to audio speakers suspending coil windings with rapidly alternating current experience Lorentz forces within an applied magnetic field creating audible variations of air pressure. The coil windings in this case are those of gradient coils and the applied magnetic field that of the scanner's static magnetic field. These vibrating gradient coils can produce noise levels as high as 97 db(A) during execution of EPI sequences in a 3.0 T scanner [41]. Noise exposure levels of 97 db(A) are typical for EPI sequences [41]. Hearing protection may be required in environments with noise levels above 85 dB(A) [42]. Fig. 2.14 maps the effectiveness of voice communication for different ambient noise levels at a range of distances between speaker and listener. The chart indicates that voice communication is impossible for ambient noise levels of 97 db(A) up to distances of about 1.5 m and remaining very difficult at shorter distances. Intercom communication is impossible at this level [43]. In Canada, hearing protection required for clinicians operating in these conditions [44] which can further inhibit communication in the vicinity of a running scanner. A viable solution has been use of third party wireless headsets by scanner room staff which suppress ambient noise but may require fiber connections run out of the scanner room using waveguide access [45, 12]. Use of
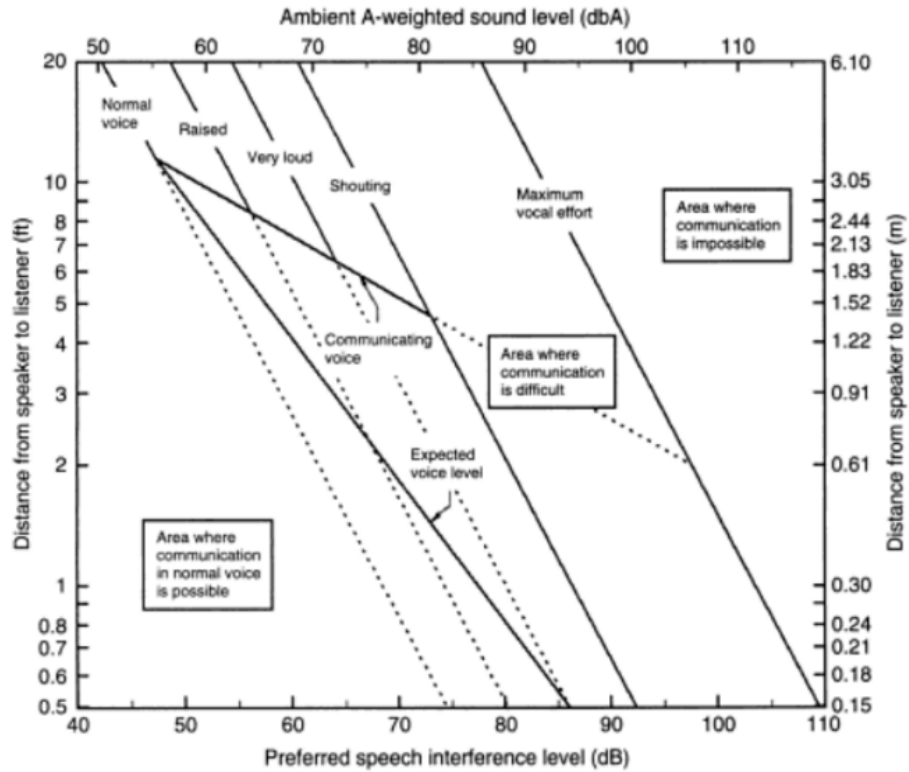
Figure 2.14: Effectiveness of voice communications as a function of ambient sound level. Taken from Davis, Jeffrey R., Robert Johnson, and Jan Stepanek, eds. Fundamentals of aerospace medicine. Lippincott Williams and Wilkins, 2008 with permission.

headsets alone do not provide a clinician with a direct means of scanner control and nevertheless require an intermediary to operate the scanner console based on verbal directions. Measuring noise levels remains an important consideration for assessing the feasibility of scanner control techniques such as that proposed by this work.

Chapter 3

Literature review

This chapter presents a literature review which describes recent work in the area of real-time imaging platforms, imaged-based localization techniques, and automated scan plane alignment. The research cited here justifies this work's main objective of developing an MR image-based localization mechanism and description is included about which aspects are incorporated into the device tracking system developed in the ensuing chapter.

3.1 Existing Interventional MRI Solutions

Specialized interventional tools have been used peripherally with modern scanner units. Active device tracking techniques include embedding RF receive coils into the construction of an interventional device connected co-axial cable link or resonant RF markers that are visualized with high signal intensity [1]. A recent example of scan plane alignment by means of active device tracking from Elayaperumal *et al.* embedded fiber optic sensors into a biopsy needle to automatically align scan planes with the needle tip, adjusting for optically sensed deflection of the needle from a rigid external base [15]. The base is tracked by means of miniature MR receiver coils localized by successive applications of frequency encoding in various directions as part of a non imaging pulse sequence. Active device tracking techniques have significant drawbacks due to safety issues such as heating of metallic components as well as the complexity and cost of incorporating tuned hardware modifications into disposable MR-safe instrumentation [46]. Philips iSuite real-time interactive interface [47] provides a fully integrated software and hardware package which can image and navigate biopsy needles in real time as shown in Fig. 3.3 (a). iSuite displays four viewports where two are updated in real time and aligned automatically to

iSuite Connectivity Diagram
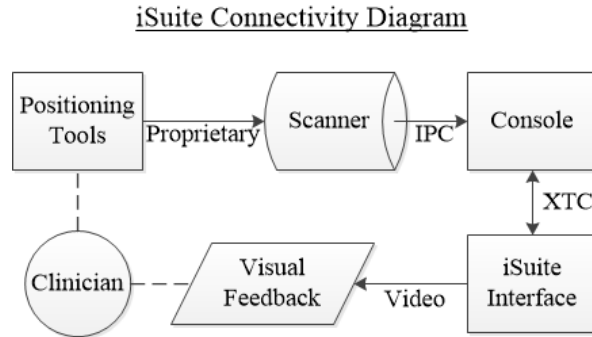
Figure 3.1: A connectivity diagram illustrates the system components of Philips iSuite.

a needle guidance tool attached to the instrument external to the patient while corresponding geometry is shown as an overlay on static scout scans in the remaining two view ports. Operator input can be collected using optically connected USB foot switch array allowing nine inputs as a three pedal array with 'short', 'long' and 'double-click' activations [48]. An interactive scanning interface running on a dedicated workstation drives foot pedal connectivity, image visualization and scanner control. The latter is implemented over Ethernet link from the dedicated personal computer (PC) to the scanner console using 'eXTernal Control' (XTC), an API for scanner connectivity [49]. A connectivity diagram for Philips iSuite is shown in Fig. 3.1.

Siemens Healthcare offers their own Interactive Front End (IFE) platform which supports modules for needle placement and thermometry compatible with various Siemens scanner models [50]. Likewise, GE Healthcare has the MR Echo interventional imaging platform [51]. Both Echo and IFE allow real-time adjustments to scan parameters such as contrast settings, image size and scan plane orientations shown in Fig. 3.2. The RTHawk platform (HeartVista, Inc., Los Altos, CA) runs with HeartVista's cardiac software package for GE scanners that allows real-time control of scan pulse sequences and acquisition but also reconstruction. This state of the art system is accessible in the scan room wirelessly through a tablet PC [12] as shown in Fig. 3.3 (b).

As described in section 1.1, MRI-guided interventions can be performed in closed bore diagnostic scanners and further discussion of scanner units will be contained within this scope. For additional information about specialized interventional scanner units, see Appendix A.1. The experiments of this work are conducted on a Philips Achieva 3.0 T closed bore scanner with a

(a)   (b)
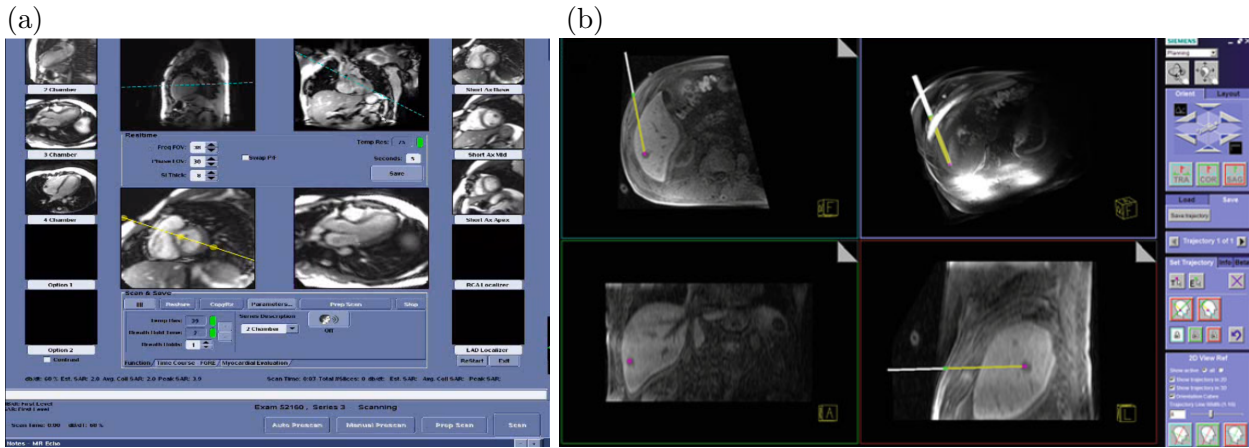
Figure 3.2: Vendor developed interventional interfaces showing real-time interactive scan plane control (a) GE MR echo screenshot (courtesy of GE Healthcare, used with permission) and (b) Siemens Interactive Front End screenshot (©2016 Siemens Healthcare GmbH. All Rights Reserved. Product photo provided courtesy of Siemens Healthcare GmbH.).

(a)   (b)
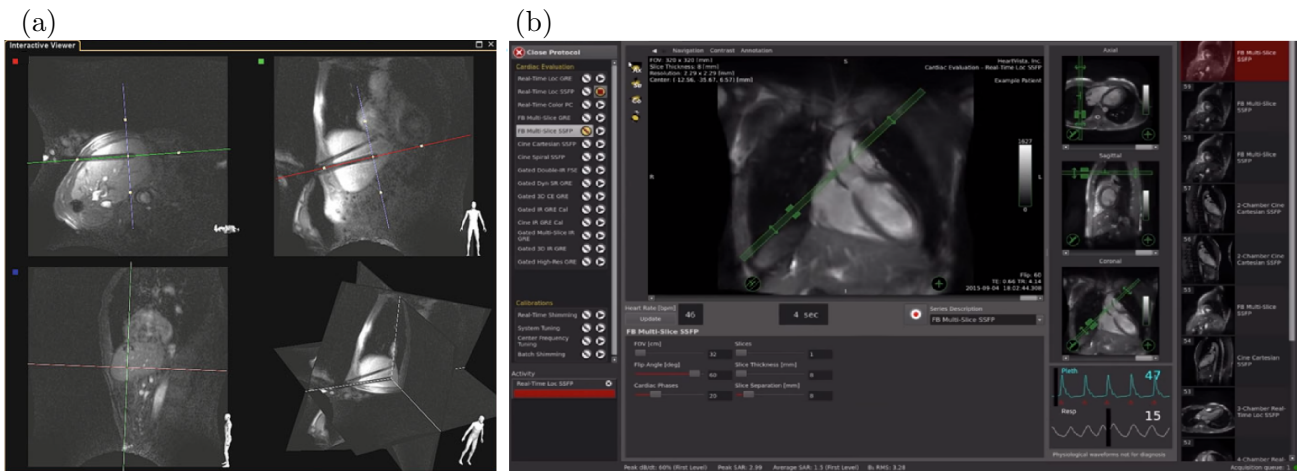
Figure 3.3: Interventional interfaces showing real-time interactive scan plane control (a) Philips iSuite screenshot (used with permission from Philips Healthcare) and (b) RTHawk user interface screenshot (used with permission of Heartvista Inc.).

gradient coil slew rate of $120 \text{ T} \cdot (\text{m} \cdot \text{s})^{-1}$ and $40 \text{ mT} \cdot \text{m}^{-1}$ respectively [52].

Active device tracking comes with significant drawbacks such as patient safety risks from device heating. Optical tracking of fiducial markers located on a needle apparatus as part of stereotactic surgical navigation can be completed within an MRI scanner bore [53]. This technique requires the markers to remain visible to navigation system cameras throughout a procedure which can be difficult or impossible to achieve given the already limited patient access inside the scanner bore. The complexity, cost and limitations of using such device tracking techniques leave a desire for device tracking techniques which do not rely on hardware modifications to interventional instruments. Although the use of actively tracked positioning tools are undesirable in view of the drawbacks mentioned, Fig. 3.1 illustrates a system design by which scanner control for a Philips scanner may be implemented and the system design of §4.3 operates on this framework.

3.2 Image-based Scan Plane Alignment

A main premise of this thesis work is that optimal scan plane geometry can be calculated based on features extracted from conditioned MRI data. Dimaio *et al.* employed algorithms for artifact detection to localize biopsy needle susceptibility artifacts from in-plane needle image data with sub-millimeter accuracy, including linear/non-linear image filters for signal conditioning and a Hugh-transform for feature extraction [54]. The same author developed a localization 'Z-frame' constructed from glass cylinders filled with MR-visible fluid. This frame exhibits a unique fiducial pattern within gradient echo images depending on the relative orientation of the frame with respect to the intersecting scan plane [55]. Localization was accomplished by convolution of fiducial k-space data with template masks to determine the best correlation with sub-millimeter and sub-degree accuracy. Localization frames have since been used for robot-assisted navigation of MRI-guided biopsies [56, 57]. An initial MR experiment established closed-loop scan plane control to maintain relative plan orientation to the 'Z-frame' as it was rotated on a moving platform inside the scanner bore or positioned with free-hand motion [58].

Chen *et al.* employed low resolution 3D scout scans for the detection of anatomical features to automatically determine the correct alignment for diagnostic brain scans [59]. The 3D scans were performed with isotropic resolution and T_1 weighted contrast to detect anatomical landmarks detected with a 'Learning Ensembles of Anatomical Patterns (LEAP)' algorithm. Landmarks are registered to a virtual atlas composed from a 'Data-adaptive Multi-structural Model (DMM)'

database trained with data from 130 adult and pediatric scans. Alignment from over 700 time trial scans verified manually to show correct orientation of the middle sagittal plane and patient brainstem in over 98% of cases with reproducible sub-millimeter and sub-degree accuracy.

3.3 MatMRI

The Philips iSuite interventional imaging platform described in §3.1 uses the XTC API for scanner connectivity [49]. This API gives client-side communication to compatible Philips scanners in the form of read access to images and corresponding meta-data as well as write access to scan parameters such as scan geometry and start/stop functionality. Networking for XTC is implemented with Common Object Request Broker Architecture (CORBA) architecture and delivered via TCP/IP. Several applications integrate XTC such as Philips Sonalleve MR-guided High Intensity Focused Ultrasound (MRgHIFU) treatment platform. CORBA software components are accessible for client programming with the 'Microsoft .Net' framework. Zaporzan *et al.* have written .Net classes (using the 'C#' programming language) and named MatMRI and MatHIFU respectively [60]. These classes are available in MATLAB and Python programming language packages (wrappers) which can interface the programs with a Philips scanner and Sonalleve systems by means of XTC.

3.4 Principal Component Analysis

Principal component analysis (PCA) is a widely used means of feature extraction within medical images [61]. Geometric applications of PCA in MRI have included determination of target displacement direction during robotic prostate biopsy [62] and automatic alignment of dynamic scan planes along directions of greatest organ tissue motion for MR-guided high intensity focused ultrasound (MRgHIFU) treatments [63]. PCA is applied in this work to calculate the spatial direction of greatest variation amongst 3D orientation scan voxels affected by the presence of an interventional device to determine its true orientation. Additional background for this topic is provided in Appendix A.2.

Chapter 4

Experiment Design

The main thesis work is set out in this chapter which describes two experiments to assess first the preliminary effectiveness of the proposed localization mechanism and secondly the feasibility of its incorporation into an interventional MRI scanner configuration. §4.1 describes a variation of principal component analysis (PCA) employed to localize a device from 3D orientation scan data, and measurements collected in §4.2 to asses the accuracy of this algorithm. §4.3 describes how this algorithm can be incorporated into interleaved scanner operation in conjunction with foot-pedal input to facilitate freehand needle placement.

4.1   Principal Component Analysis

PCA is a widely used tool for statistical analysis of multivariate data in which linearly independent factors (principal components) are calculated as a basis upon which observations can be projected to exhibit the greatest variation [64]. These orthogonal components consist of linear combinations of the original p variables. Principal component vectors $\mathbf{U} = \left(\hat{\mathbf{u}}^{(1)}, \hat{\mathbf{u}}^{(2)}, \dots , \ \hat{\mathbf{u}}^{(p)}\right)^1$ can be calculated from the singular value decomposition of a symmetric observation data covariance matrix $\mathbf{C}$ where:

$$\mathbf{C} = \frac{1}{n}\mathbf{R}\mathbf{R}^T = \mathbf{U}\mathbf{\Lambda}\mathbf{U}^T \tag{4.1}$$

with mean-centered observation data input matrix $\mathbf{R} = (\mathbf{r}^{(1)}, \mathbf{r}^{(2)}, \dots , \mathbf{r}^{(n)}) \in \mathbb{R}^{p \times n}$ and $\mathbf{\Lambda} = \mathbf{diag}(\boldsymbol{\lambda})$ is a diagonal matrix of eigenvalues $\boldsymbol{\lambda} = (\lambda_1, \dots , \lambda_p)$ [65].

The centroid and direction of greatest spatial variation among tissue voxels affected by the presence of an interventional device allow the device position and orientation to be calculated

---

[1]Vectors noted in this work are designated as column matrices.
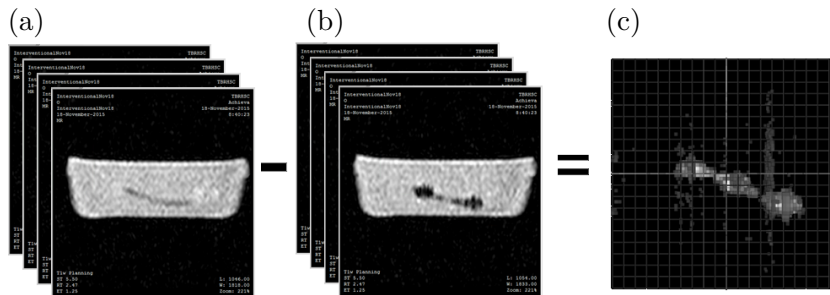
Figure 4.1: Element-wise subtraction of 3D orientation image data sets produces artifact position observation data with additional magnitude information.

respectively. These voxels comprise the device signal void, and as well as susceptibility effects of spatial distortion and dephasing [19]. To determine the coordinates of affected voxels as three dimensional observations for PCA, element-wise subtraction of two 3D image data sets reconstructed from rapid orientation acquisitions is proposed as illustrated in Fig. 4.1. Here, we see (a) a 3D orientation image data set acquired after partial placement of an MR-compatible catheter device within a gelatin phantom subtracted from (b) a baseline 3D orientation image data set acquired before placement to produce (c) 3D artifact coordinate data with additional magnitude information. The observations are segmented based on percentile rank calculated from the absolute change in magnitude for each voxel, effectively thresholding observations to a fixed number $m = \frac{n \cdot \Gamma}{100\%}$ where $\Gamma \in [0, 100]\%$ and n is the total number of elements in the orientation scan reconstruction matrix. The computational cost of this operation is calculated from sorting and slicing operations [66] to give:

$$O(n \cdot log(n) + m). \tag{4.2}$$

The computational complexity of completing a principal component analysis is dominated by the covariance matrix calculation with $O(mp^2)$ [67] where m is the number of observations. Subsequent calculation of eigenvectors as principal component vectors from the covariance matrix by singular value decomposition comes with an additional computational cost of $O(p^3)$ [68]. The combined computational cost is given by:

$$O(mp^2 + p^3) \approx O(m), \qquad m \gg p. \tag{4.3}$$

The contribution of a given observation to the calculation of each component increases with

squared distance from the sample mean in terms of its factor score [69, 64] according to Eq. 4.4. The contribution $\psi_{i,j}$ of i-th factor score f to the calculation of component j with associated eigenvalue λ_j is given by:

$$\psi_{i,j} = \frac{f_{i,j}^2}{\sum_k^n f_{k,j}^2} = \frac{f_{i,j}^2}{\lambda_j} \tag{4.4}$$

where $f_{i,j} = \left(\hat{\mathbf{u}}^{(j)}\right)^T \mathbf{r}^{(i)}$ and $\lambda_j = \sum_k^m f_{k,j}^2$. Pixel magnitude information corresponding to each observation can be regarded as the sum of binary signal states located within the boundaries of the voxels from which pixels are reconstructed. To account for this sum with PCA, each unique observation can be replicated according to a factor $w_i \in \mathbb{N}$. Values of w_i are chosen a linearly proportional to the corresponding pixel intensity of each observation. The combined contribution $\psi_{i,j}^c$ of the i-th unique observation to principal component j given by Eq. 4.4 becomes:

$$\psi_{i,j}^c = \frac{w_i f_{i,j}^2}{\sum_k^m w_k f_{k,j}^2} \tag{4.5}$$

$$= \frac{\left(\sqrt{w_i} f_{i,j}\right)^2}{\sum_k^m \left(\sqrt{w_k} f_{k,j}\right)^2}. \tag{4.6}$$

Eq. 4.6 indicates that replication effectively scales factor scores according to $\sqrt{w_i}$. Simple replication of input data is undesirable according to Eq. 4.3 such that m increases to $\sum w_i$. To achieve this effect with a fixed number of computations, the observation covariance matrix $\mathbf{C}$ is shown to require a weighted input matrix $\mathbf{S} = \left(\mathbf{s}^{(1)}, \dots, \mathbf{s}^{(m)}\right)$:

$$\mathbf{C} = \frac{1}{\Sigma w_i} \sum_{i=1}^m w_i \left(\mathbf{r}^{(i)} - \bar{\mathbf{s}}\right) \left(\mathbf{r}^{(i)} - \bar{\mathbf{s}}\right)^T \tag{4.7}$$

$$= \frac{1}{\Sigma w_i} \mathbf{Q}\mathbf{W}\mathbf{Q}^T = \frac{1}{\Sigma w_i} \left(\mathbf{Q}\mathbf{W}^{1/2}\right) \left(\mathbf{Q}\mathbf{W}^{1/2}\right)^T \tag{4.8}$$

$$= \frac{1}{m} \mathbf{S}\mathbf{S}^T \tag{4.9}$$

$$\therefore \mathbf{S} = \sqrt{\frac{m}{\Sigma w_i}} \mathbf{Q}\mathbf{W}^{1/2} \tag{4.10}$$

where

$$\mathbf{Q} = \left(\mathbf{r}^{(1)} - \bar{\mathbf{s}}, \dots, \mathbf{r}^{(m)} - \bar{\mathbf{s}}\right) \tag{4.11}$$

$$\bar{\mathbf{s}} = \frac{\sum w_i \mathbf{r}^{(i)}}{\sum w_i} \tag{4.12}$$

and $\mathbf{W} = \mathbf{diag}(\mathbf{w})$ is a diagonal matrix of the factor score coefficients $\mathbf{w} = (w_1, ..., w_m)$. The complexity of arithmetic operations required to calculate the weighted input matrix is simply $O(m)$. Eq. 4.10 shows how no initial estimate is required in this case, however an iterative method could be used if scaling was not equal across all components [70]. The overall procedure is shown in Algorithm 1 given the number of observations to segment m out of n total observations. The

Input: m

Data: $\mathbf{R} = (\mathbf{r}^{(1)}, ..., \mathbf{r}^{(n)})$, $\mathbf{w} = (w_1, ..., w_n)$

Result: $\hat{\mathbf{u}}^{(1)}$, $\bar{\mathbf{s}}$

// Find indices of top 'm' voxels

for $t = 1, 2, ..., m$ **do**

$\quad$ choose $i_t \in \mathbb{N} : \frac{\text{percentile rank}\{w_{i_t}\}}{100\%} > \left(1 - \frac{m}{n}\right)$

end

// Weight observation matrix

$\bar{\mathbf{s}} = \frac{\sum_{t=1}^{m} w_{i_t} \mathbf{r}^{(i_t)}}{\sum_{t=1}^{m} w_{i_t}}$

for $t = 1, 2, ..., m$ **do**

$\quad$ $\mathbf{s}^{(t)} = \sqrt{w_{i_t}} \left(\mathbf{r}^{(i_t)} - \bar{\mathbf{s}}\right)$

end

// Calculate adjusted PCA

$\mathbf{C} = \frac{1}{m} \sum_{t}^{m} (\mathbf{s}^{(t)})(\mathbf{s}^{(t)})^T = \mathbf{U}\mathbf{\Lambda}\mathbf{U}^T$

Algorithm 1: Adjusted principal component analysis with scaled observations.

desired outputs of this algorithm are the first principal component $\hat{\mathbf{u}}^{(1)}$ obtained by singular value decomposition according to Eq. 4.1 and position centroid $\bar{\mathbf{s}}$. i_t are the indices of segmented observations. From Eq. 4.3 and Eq. 4.2, the combined computational cost of the entire process is summarized by

$$O(n \cdot log(n) + m + mp^2 + p^3) \approx O(n \cdot log(n)), \quad n \gg m \gg p. \tag{4.13}$$

4.2 Preliminary Effectiveness Study

Preliminary evaluation of the of the proposed algorithm's effectiveness was conducted using a Philips Achieva 3.0 T scanner running Philips MR release 3.2.3. Software restrictions limited 3D acquisition matrices to a minimal size of $64 \times 64 \times 64$ when configuring isotropic scan parameters

Table 4.1: Parameters selected for orientation scans during the preliminary effectiveness study.

Scan Number	1	2	3	4
T_R (ms)	4.5*	37.8	105.0	205.8
T_E (ms)	1.9	2.1	2.1	2.2
Scan Time (s)	14.6	121.0	337.2	660.8
Flip Angle (°)	4.5	13.16	21.76	30.1

for 3D orientation scan acquisitions. To avoid influence from interpolation effects on orientation data during reconstruction, the reconstruction matrix was also chosen as $64 \times 64 \times 64$ corresponding to an input data size of $n = 64^3$. Contrast between tissues was not needed for these scans, but instead contrast between the signal void created by the device and the surrounding tissue. This proton density (ρ) weighting requires a relatively long repetition time and relatively short echo time [17] where $T_R \sim T_1$ and $T_E \ll T_2$.[2] Achieving proton density weighting shares a common requisite with increasing SNR according to Eqs. 2.10 and 2.11, but also requires an increase in acquisition time. A range of T_R values was selected corresponding to theoretical linear increases of SNR and listed in Table 4.1 to explore the trade-off between algorithm performance and required scan time.

No signal averaging was performed to minimize total scan duration. Magnitude image data from these 3D acquisitions was formatted as 64 coronal slices. Remaining MR parameters were selected to optimize containment of a 310 mm-long, 11-gauge titanium biopsy needle with a 7 mm-bevel tip. A rigid frame of polystyrene was constructed to ensure that the biopsy needle was placed into a porcine shoulder specimen with a double oblique orientation of 14° and 12° from the sagittal and coronal planes respectively. This corresponds to an needle angle of $\beta = \alpha = 18.4°$ from the shared static magnetic field and frequency encoding axis. The head/foot direction was chosen for frequency encoding to minimize spatial distortion external to the needle according to Eq. 2.6. Flip angles were calculated based on a typical T_1 value for muscle tissue at $3.0T$ [71] using the Ernst angle α_E given by

$$\alpha_E = \arccos\left[\exp\left(-T_R/T_1\right)\right]. \tag{4.14}$$

A field of view of $128 \times 128 \times 128$ mm^3 was chosen for a resolution of $2 \times 2 \times 2$ mm^3. To evaluate

---

[2]Here, T_1 and T_2 are taken as the magnetic relaxation time constants of surrounding tissues.

Table 4.2: Parameters selected for accelerated orientation scans during the preliminary effectiveness study.

Scan Number	5	6	7	8
T_R (ms)	4.4*	37.8	105.0	205.8
T_E (ms)	2.1	2.1	2.1	2.2
Scan Time (s)	4.6	39.4	109.0	214.6
Flip Angle (°)	4.5	13.16	21.76	30.1

the performance of the proposed algorithm using accelerated image techniques, a second table of scan parameters was selected based on a half-scan ratio of 0.625 and a reconstruction matrix of $64 \times 64 \times 64$ with an acquisition matrix of $64 \times 64 \times 32$ and a voxel size of $2 \times 2 \times 4$ mm^3, as shown in Table 4.2. The field of view remained unchanged.

The scan protocol described by Tables 4.1 and 4.2 was also performed devoid of needle placement to provide a baseline from which orientation scans may be subtracted to produce data for Algorithm 1. Actual needle placement was verified with localizer scans with parameters $T_R = 11$ ms, $T_E = 5$ ms, flip angle = 15°, slice thickness = 10 mm, FOV = 250×250 mm^2, acquisition matrix = 256×128, and reconstruction matrix = 256×256.

4.3 Feasibility Study

Trials were conducted with an experimental set-up demonstrated with previous experiments [72] and illustrated in Fig. 4.2. Trials were conducted with the experimental setup illustrated in Fig. 4.2 using a Philips Achieva 3.0 T scanner, an 11-gauge titanium biopsy needle, and an MR safe projector unit (MRA Inc., Washington, PA, USA). Operator input was collected using foot-pedal optical switches constructed with plastic and brass to interrupt a 5 mW, 650 nm multi-mode fiber optic circuit interfaced with an external control PC. The foot pedal layout was based on a footswitch for the Artis-Zeego interventional fluoroscopy imaging system (Siemens Healthcare, Erlangen Germany) and illustrated in Fig. 4.3. The layout contains two elevated push-button switches and a dual rocker style foot switch. The status of individual switches on the array is sensed by photodiode components (Industrial Fiber Optics Inc., Tempe, AZ, USA) and detected by microcontroller unit (MCU) (Arduino LLC, Somerville, MA, USA). The

---

* Values result from 'Shortest TR' option selected within Philips MR release 3.2.3
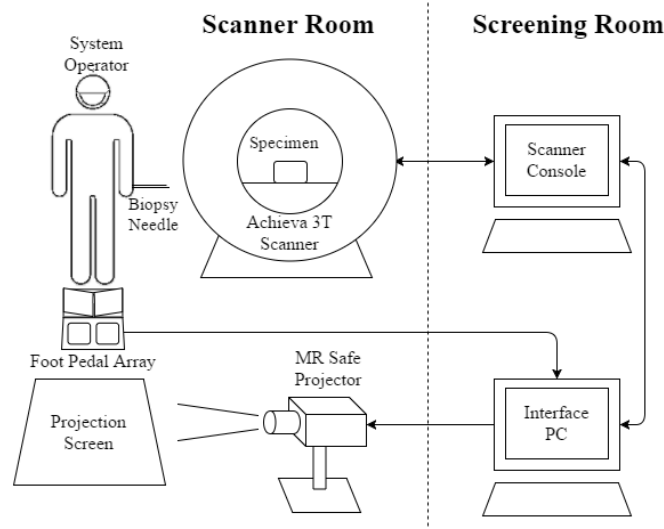
Figure 4.2: Diagram of equipment configuration used for subsequent experiments.

MCU is programed in a loop to check each switch state upon query and transmit a priority encoded status code asynchronously to a host workstation by means of virtual serial port over USB. Fig. 4.4 shows a schematic for the fiber optic transceiver constructed to interface the external control PC with a 1000 μm diameter by 20 m long circuit. A GUI application was written in the Python computer language to control the scanner according to operator input using the MatMRI software toolbox. This application was also used to display a visualization of the procedure inside the scanner room using the connected projector. Three views were aligned horizontally according to Fig. 4.5 with primary transverse view[3] (left) and auxiliary coronal and sagittal oblique views (centre and right). Image overlay information was included with images to display a scan time stamp collected at the scanner host as well as image plane coordinates. The time stamp values collected from metadata headers were comparable to DICOM address [0008,0032] and [0008,0033] which indicated the time at which imaging is initiated. The image plane coordinates refered to the centre of the imaging plane with respect to the scanner coordinate system originating at the scanner isocenter and patient axes. Direction indicators are placed to ensure an operator's familiarity with the orientation of each image plane. Images from each session are stored automatically and available for review using the same interface. A flow chart

---

[3]In this work, 'transverse' refers to the patient anatomical plane so as to avoid confusion with 'axial' images of a needle cross section not necessarily oriented parallel to the transverse plane.
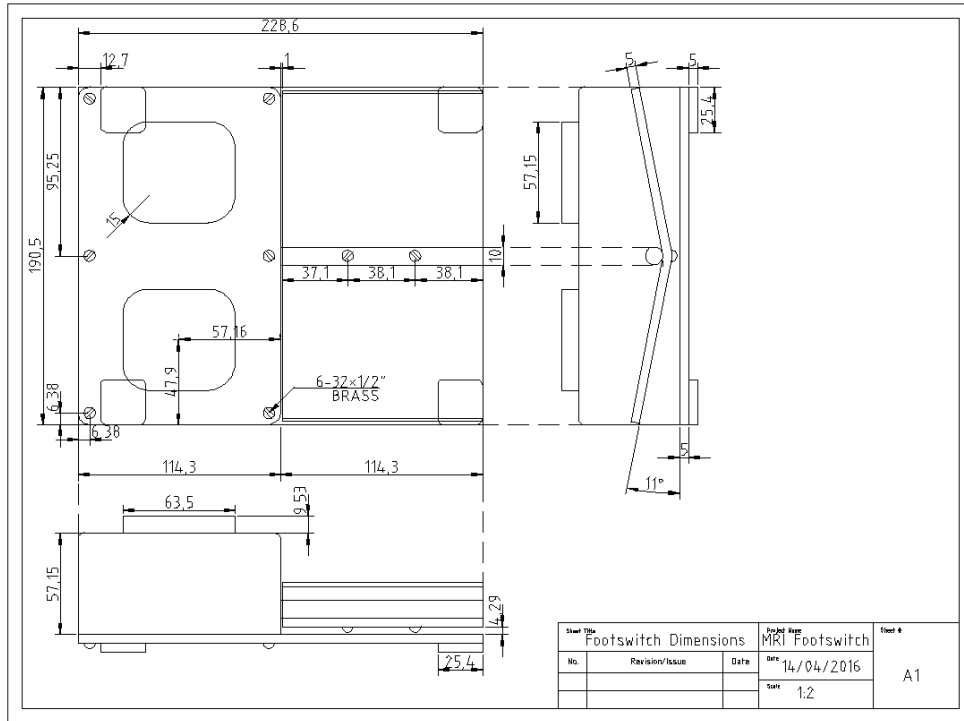
Figure 4.3: Layout drawing for MR-compatible footswitch array.
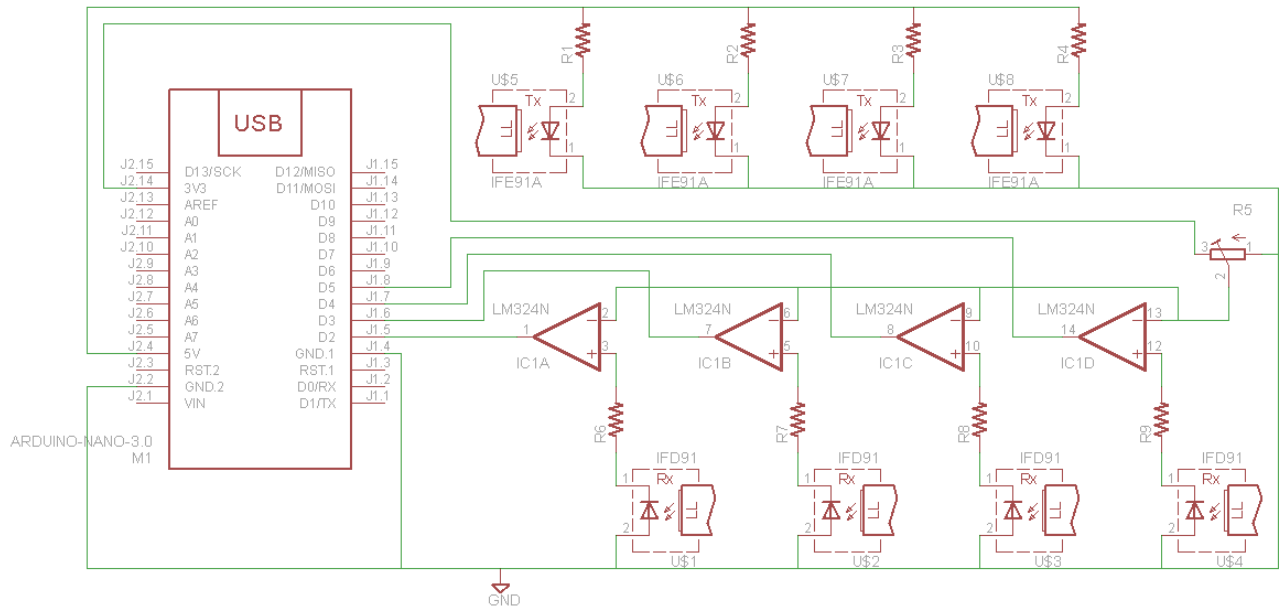
Figure 4.4: Schematic drawing of a fiber optic transceiver interface.
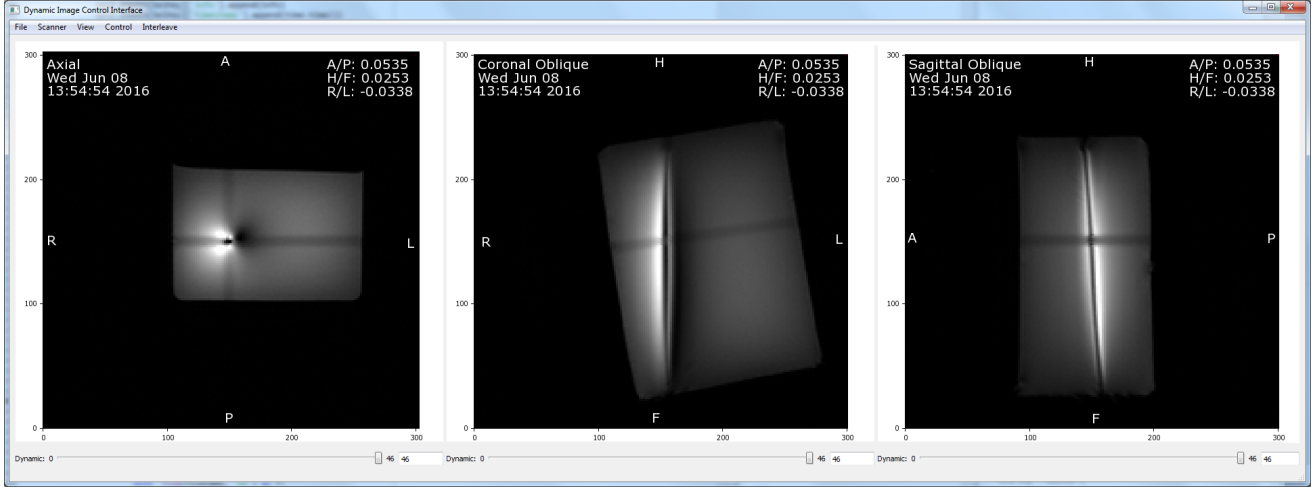
Figure 4.5: Screenshot of interface system software GUI while in operation.

depicting the basic operation of the real-time MR scanner control GUI is shown in Fig. 4.6. The 3D orientation scans described in §4.2 were interactively inserted into a time interleaved scan protocol using MatMRI to update MR sequence parameters [73]. Repetition settings for image frames within an interleaved cycle could be toggled on demand between the two configurations shown in table 4.5 so as to trigger a single orientation scan between real-time visualization image frames.[4] A master-slave implementation of interleaved scanning for Philips MR release 3.2.3 limited the minimum number of repetitions of visualization scans to one per interleaved cycle. Visualization parameters were based on a set for real-time interactive multi-slice visualization of needle placement taken from Rothgang *et al.* [29] and noted in Table 4.3.

Orientation scan parameters were chosen according *Scan #1* results noted in Table 5.1 reducing orientation scan time acquisition time to 14.6 s and minimizing workflow interruption. From Eq. 2.9, using $d = 4$ mm, $e_\theta = 0.39°$pp, $e_{\bar{s}} = 2.38$ mm and ROI $= 128$ mm (corresponding to the orientation scan field of view), a biopsy needle can be fully visualized across an ROI of 180 mm. All scanning was performed using the scanner body coil. These configurations were incorporated into each trial according Fig. 4.7 and Fig. 4.8. Scanning initiated with a single cycle of interleaving configuration B for the collection of a baseline scan which served as a reference from which subsequent orientation scans were subtracted according to §4.2. Upon each foot pedal command

---

[4]Here, the term 'image frame' describes a multi-stack acquisition with at least one slice per stack.
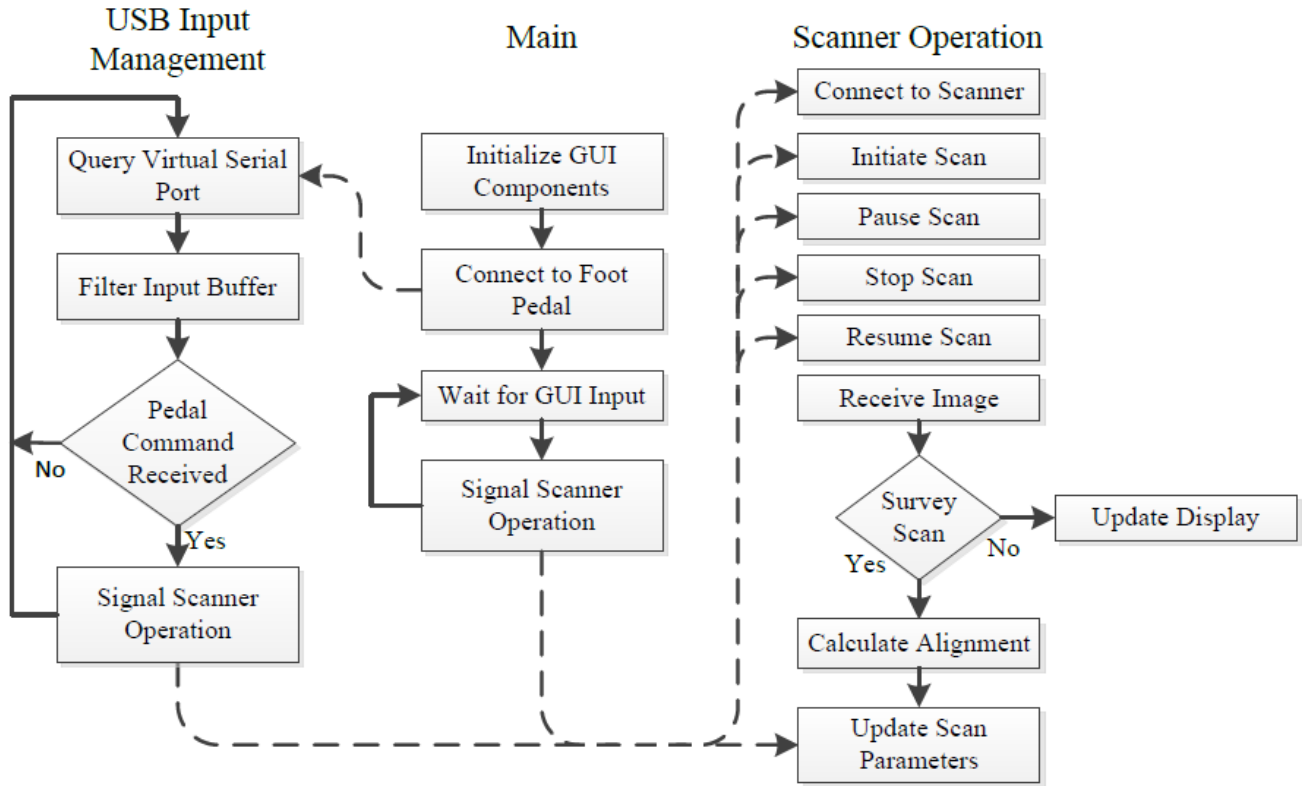
Figure 4.6: A flow chart depicting the basic operation of the real-time MR scanner control GUI. Dashed lines indicate creation of a parallel thread.

Table 4.3: Parameters selected for visualization scans.

Parameter	Value
TR	17.6 ms
TE	2.3 ms
Flip angle	30°
Slice thickness	10 mm
FOV	300×300 mm^2
Acquisition matrix	192×192
Stacks	1
Slices/stack	3
Time/frame	2.7 s for three frames

Table 4.4: Parameters selected for orientation scans.

Parameter	Value
TR	4.5 ms
TE	1.9 ms
Flip angle	4.5°
FOV	$128 \times 128 \times 128$ mm^3
Acquisition matrix	$64 \times 64 \times 64$
Time/frame	14.6

Table 4.5: Repetition configurations for interleaved scanning.

	Repetitions Per Cycle	
	Visualization	Orientation
Configuration A	1	0
Configuration B	1	1

from the system operator, a single cycle of configuration B was queued for immediate execution. Complete acquisition of an orientation scan preceded calculation of new geometry parameters during the remainder of the interleaving cycle. The new parameters were calculated according to Algorithm 1 as well as Eqs. 4.16-4.19 and applied instantly upon restoration of interleaving configuration A. Orientation scan image data was scaled according to XTC meta-data rescale slope and rescale intercept values (analogous to DICOM address [0028,1052] and [0028,1053] respectively) before application of the algorithm as is required for normalization of magnitude values received from the Philips Achieva 3.0 T [74, 75]. The time required for a complete cycle T_c of Configuration B and thus the time required to complete scan plane re-alignment is given by:

$$T_c = \tau_1 + \tau_2 \tag{4.15}$$

Where τ_1 is the time required to obtain one orientation scan image frame (one complete 3D acquisition) and τ_2 is the time required to obtain one visualization scan image frame (one complete multi-stack acquisition). These times are specified in Tables 4.4 and 4.3.

Fig. 4.9 (a) illustrates the multi-stack scan plane configuration used for needle visualization given a needle alignment vector $\hat{\mathbf{u}}^{(1)}$ calculated with Algorithm 1. Fig. 4.9 (b) labels the required
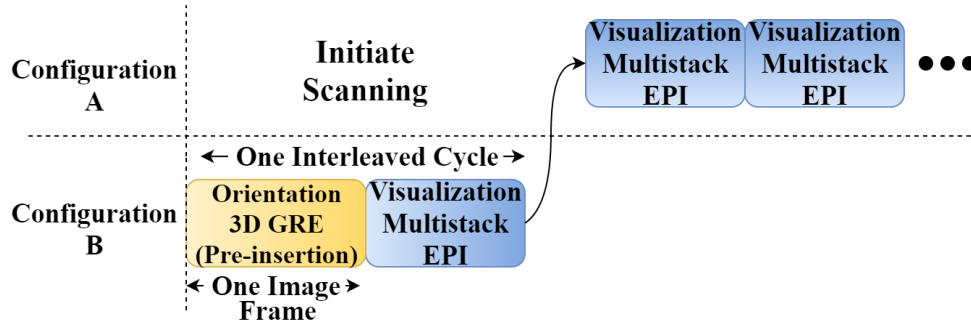
Figure 4.7: A time-interleaved scan protocol for initiating scanning as part of the proposed alignment technique.

Figure 4.8: A time-interleaved scan protocol for interactively inserting a single orientation scan between visualization scans in order to calculate and apply new geometry parameters.
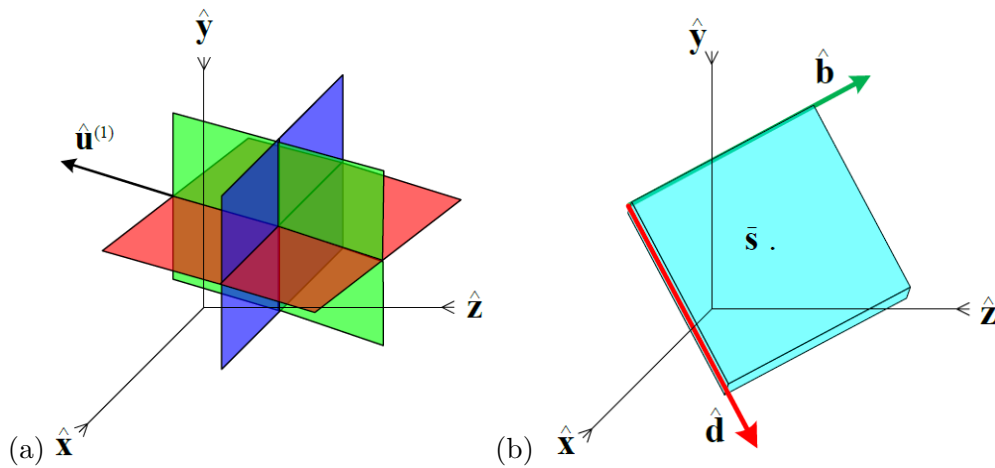
Figure 4.9: Illustrations of (a) multi-stack dynamic scan plane configuration and (b) orientation vectors that define the geometry of a given slice.

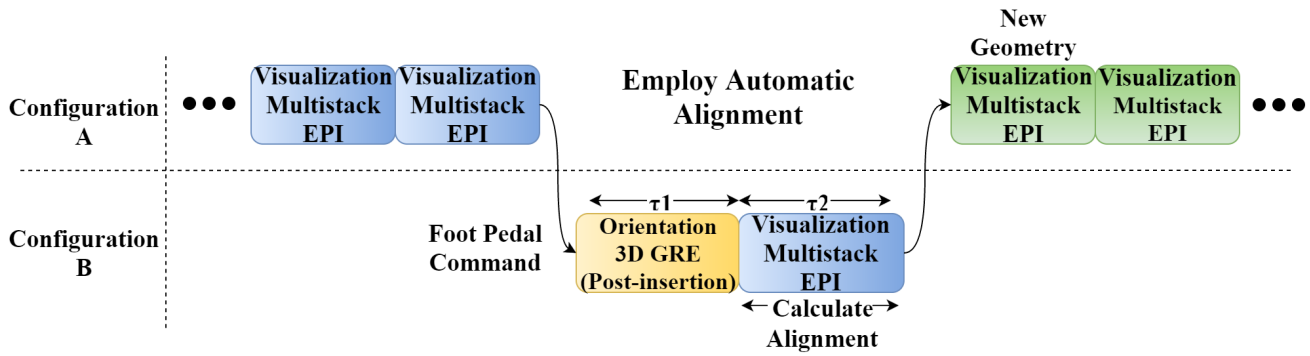vectors to determine an individual image slice orientation with orthogonal $\hat{\mathbf{b}}$ row and $\hat{\mathbf{d}}$ column vectors relative to the scanner coordinate system and centre position calculated as a weighted centroid of segmented observations according to Eq. 4.12. Eqs. 4.16-4.19 show how row and column vectors for coronal oblique (red), sagittal oblique (green) and transverse (blue) scan planes are obtained for this designated with c, s, and t subscripts respectively. $\hat{\mathbf{x}}$, $\hat{\mathbf{y}}$ and $\hat{\mathbf{z}}$ vectors represent right-left, anterior-posterior and foot-head patient axes.

$$\hat{\mathbf{d}}_c = \hat{\mathbf{d}}_s = -\frac{\hat{\mathbf{u}}^{(1)}}{||\hat{\mathbf{u}}^{(1)}||} \tag{4.16}$$

$$\hat{\mathbf{d}}_t = \hat{\mathbf{y}} \tag{4.17}$$

$$\hat{\mathbf{b}}_c = \frac{\hat{\mathbf{u}}^{(1)} \times \hat{\mathbf{x}}}{||\hat{\mathbf{u}}^{(1)} \times \hat{\mathbf{x}}||} \tag{4.18}$$

$$\hat{\mathbf{b}}_s = \frac{\hat{\mathbf{u}}^{(1)} \times \hat{\mathbf{y}}}{||\hat{\mathbf{u}}^{(1)} \times \hat{\mathbf{y}}||} \tag{4.19}$$

$$\hat{\mathbf{b}}_t = \hat{\mathbf{x}} \tag{4.20}$$

A rigid frame of polystyrene was obtained with inner dimensions measuring $22.0 \times 16.5 \times 13.0$ cm^3 in the head-foot, left-right, anterior-posterior directions respectively and designated as *frame #1*. The frame contained a gel phantom created with 5.93 g $\cdot$ L^{-1} gelatine powder congealed with water. A 6 ml vial of water containing 4.27 mmol $\cdot$ L^{-1} gadoteridol was inserted into the centre of phantom. An additional frame of polystyrene was obtained with inner dimensions measuring $20.3 \times 16.5 \times 19.0$ cm^3 in the head-foot, left-right, anterior-posterior directions respectively and designated as *frame #2*. A porcine left shoulder specimen containing skin, fat, bone and muscle tissue was procured to fit the inner dimensions of the frame. A 12 ml vial of water containing 0.32 mmol $\cdot$ L^{-1} was inserted into the centre of specimen.

Un-trained operators (N=3) each participated in two separate trials. The first trial was completed using frame #1 and the second using frame #2. During each trial, the operators manually guided the provided biopsy needle tip from arbitrary entry sites of the foot end of the frame using freehand placement to target a location specified as the conical tip of either vial containing contrast-enhanced fluid as illustrated in Fig. 4.10. Operators were positioned on the right side (patient left) of the patient table. Visualization during trials was projected onto a backing situated on the left side (patient right, according to DICOM patient axes which assume supine
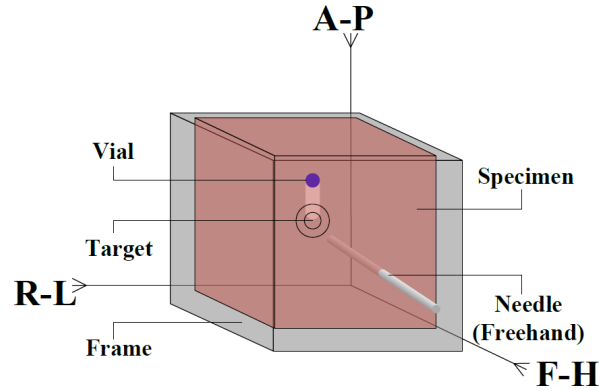
Figure 4.10: A diagram illustrates needle placement during time trials. Actual frames were opaque and occluded view of the enclosed specimen.

positioning of the scanner subject) directly adjacent to the opening of the scanner bore. Final needle tip distance from the target and scan plane alignment were verified using localizer scans with parameters $T_R = 55$ ms, $T_E = 2$ ms, flip angle = 30°, slice thickness = 10 mm, FOV = 250×250 mm^2, acquisition matrix = 128×128, and reconstruction matrix = 256×256. Operators wore two levels of hearing protection: earplugs with NRR = 33 (3M Inc., St. Paul, MN, USA) and earmuffs with NRR ~ 30 (Koninklijke Philips N.V., Netherlands).

Chapter 5

Results and Analysis

5.1 Preliminary Effectiveness Study

Fig. 5.1 shows the centroid position ($\bar{\mathbf{s}}$) error for each scan. The average error across all scans reaches a minimum at a threshold value of $\Gamma = 0.21\%$, marked in Fig. 5.2 corresponding to $m = 551$ observations with which the line fitting results of Fig. 5.3, Fig. 5.6 and Fig. 5.7 as well as Table 5.1 were calculated. In the region shown, threshold values exhibit a direct relationship to the mean radial distance of observations to the needle axis with a correlation coefficient of $r = 0.996$. Fig. 5.3 shows a 3D rendering of the line fitting results from Algorithm 1 super-imposed over point cloud observations thresholded at a higher value for illustration. The transparency of each point in the cloud is rendered according to the corresponding value of w_i. Longitudinal and lateral angle results for individual scans are shown in Fig. 5.4 and Fig. 5.5 respectively. SNR measurements are shown for all scans before baseline subtraction in Table 5.1, calculated using the conventional ROI method [76] over the same regions for each scan. Line fittings are individually projected onto the axis of the needle in Fig. 5.6 and Fig. 5.7 along with corresponding point cloud data. The grid size markings are set according to the orientation scan voxel size. Patient coordinate axes shown are oblique according to the acute angles of the needle orientation. An ideal line-fitting result here would be illustrated as a single dot in the centre of the plot. Fig. 5.8 shows the transverse plane intersection of the inserted biopsy needle artifact within the porcine shoulder specimen. A smaller signal void from a prior placement is also visible. Computation time is measured on an Intel(R) Xeon(R) CPU at 2.13 GHz with 12.0 GB RAM and recorded in Table 5.1. H,F,L,R,A,P designations correspond to Head, Foot,
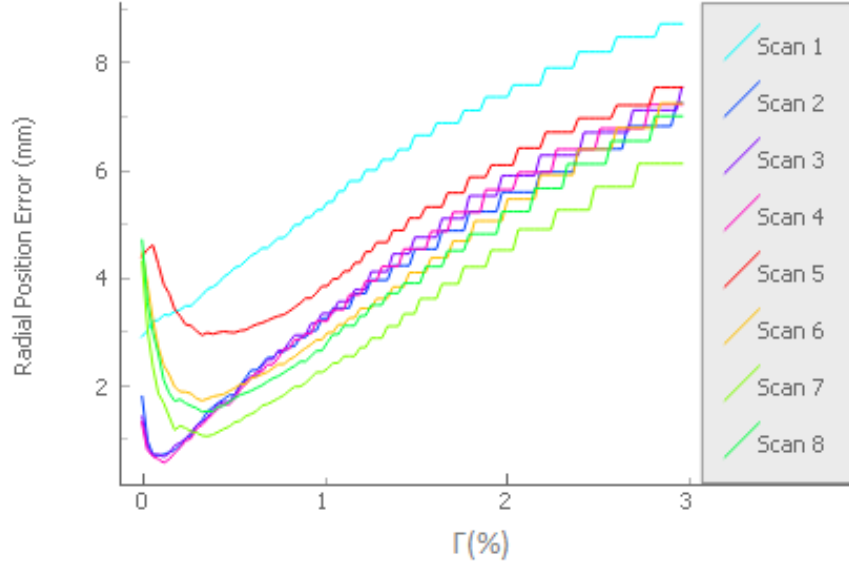
Figure 5.1: Mean centroid position error of individual scans as a function of threshold value.

Table 5.1: Results and measured SNR for each scan with $\Gamma = 0.21\%$.

Scan Number	1	2	3	4	5	6	7	8
SNR	21.39	57.34	68.03	97.91	16.09	22.02	24.39	25.26
Lateral Position Error (mm)	-2.38	0.11	0.28	0.30	-1.83	-0.76	-0.45	-0.78
Longitudinal Position Error (mm)	2.36	0.79	0.83	0.68	2.88	1.79	1.04	1.50
Lateral Angular Error (°)	0.34	0.22	0.05	0.04	-0.07	0.89	1.33	0.78
Longitudinal Angular Error (°)	-0.39	-0.26	-0.2	-0.22	-0.6	-0.22	-0.05	-0.375
Computation Time (ms)	10	9	7	8	9	9	8	7

Left, Right, Anterior, and Posterior patient directions respectively for all figures.

5.2 Feasibility Study

The mean targeting error was in-plane and out-of-plane errors were calculated from verification scan image data on the basis of coronal planes. The actual needle tip location was manually determined from verification data as the focal point of signal dephasing around the end of the needle artifact. The mean targeting error across all directions was 3.6 mm and 5.1 mm for the phantom trials and *ex-vivo* trials respectively. The average entry-to-target time was 247 sec. 83% of trials resulted in the needle resting in physical contact with the target vial. Table 5.3 compares trial times from the feasibility experiment results to those of a similar fixed-plane
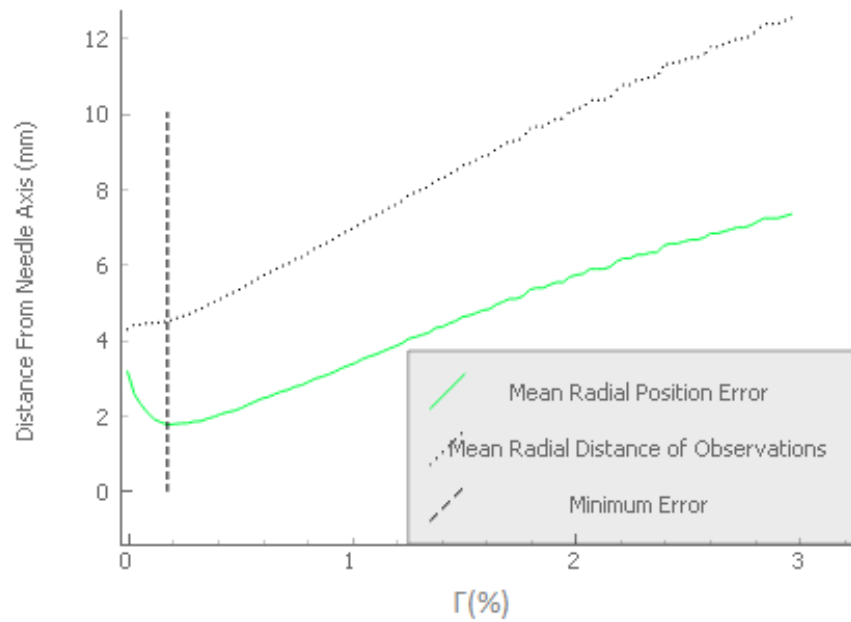
Figure 5.2: Mean centroid position error and distance of individual observations averaged across all scans as a function of threshold value.
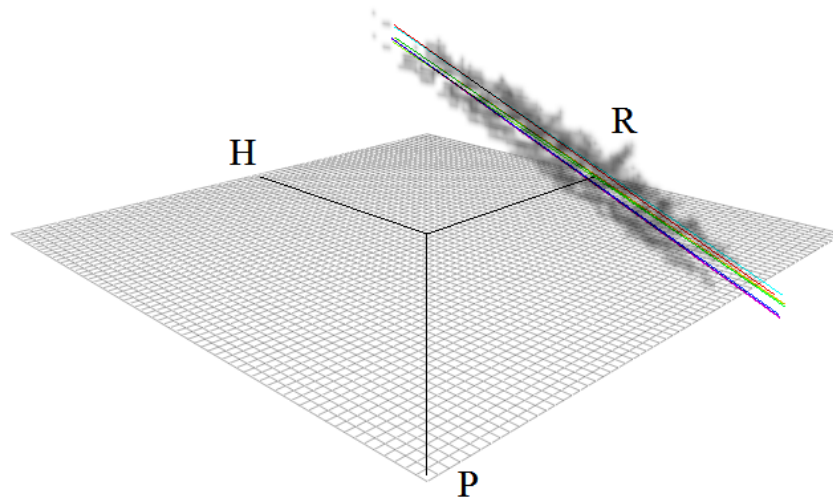
Figure 5.3: Algorithm line fitting results for all scans calculated with $\Gamma = 0.21\%$ superimposed over point-cloud data from scan two segmented with $\Gamma = 0.21\%$.
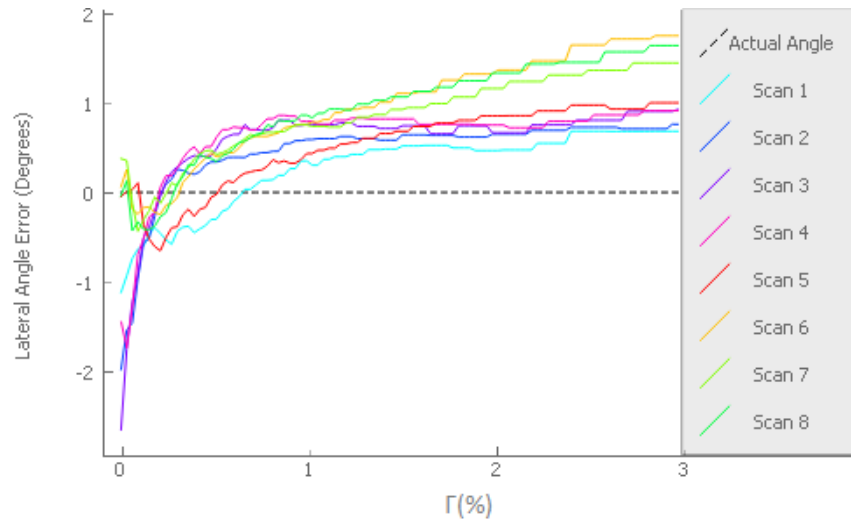
Figure 5.4: Lateral angle of line fittings plotted as a function of threshold value.
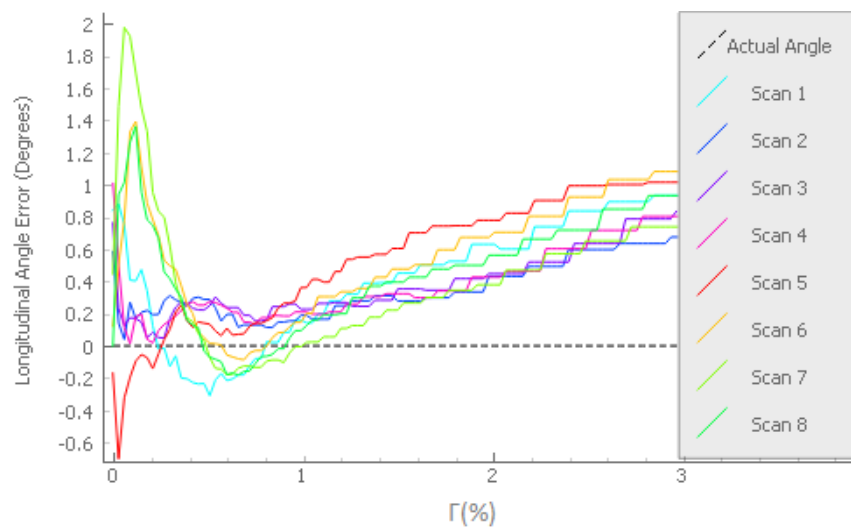
Figure 5.5: Longitudinal angle of line fittings plotted as a function of threshold value.
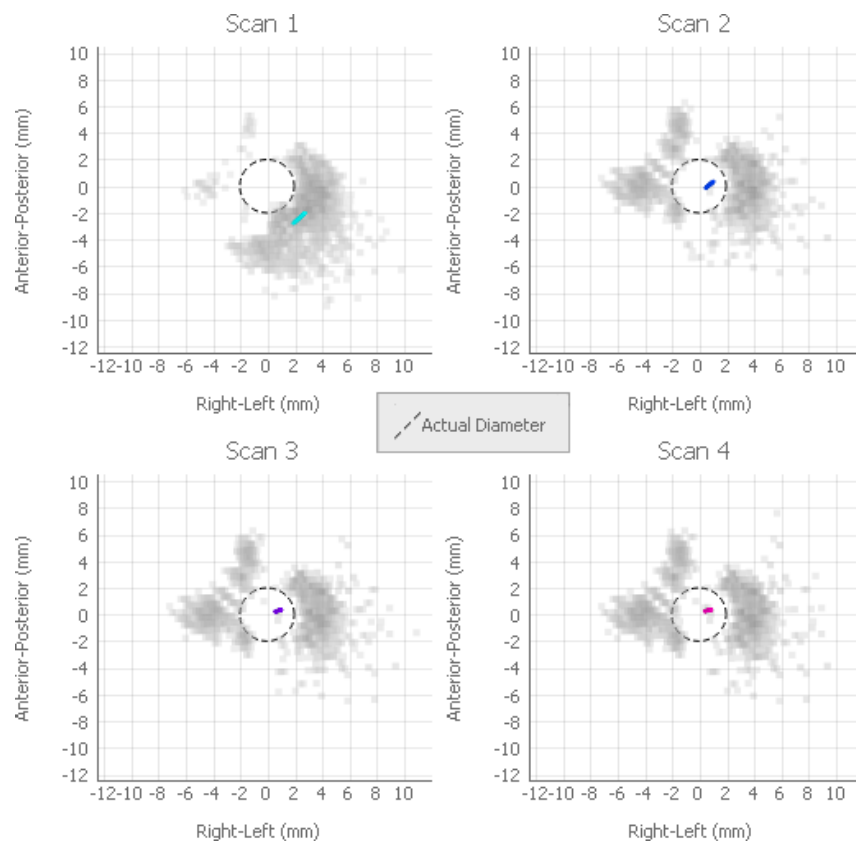
Figure 5.6: Line fitting results (coloured) and point-cloud data thresholded with $\Gamma = 0.21\%$ from scans 1-4 projected onto the needle axis with $\Gamma = 0.21\%$.
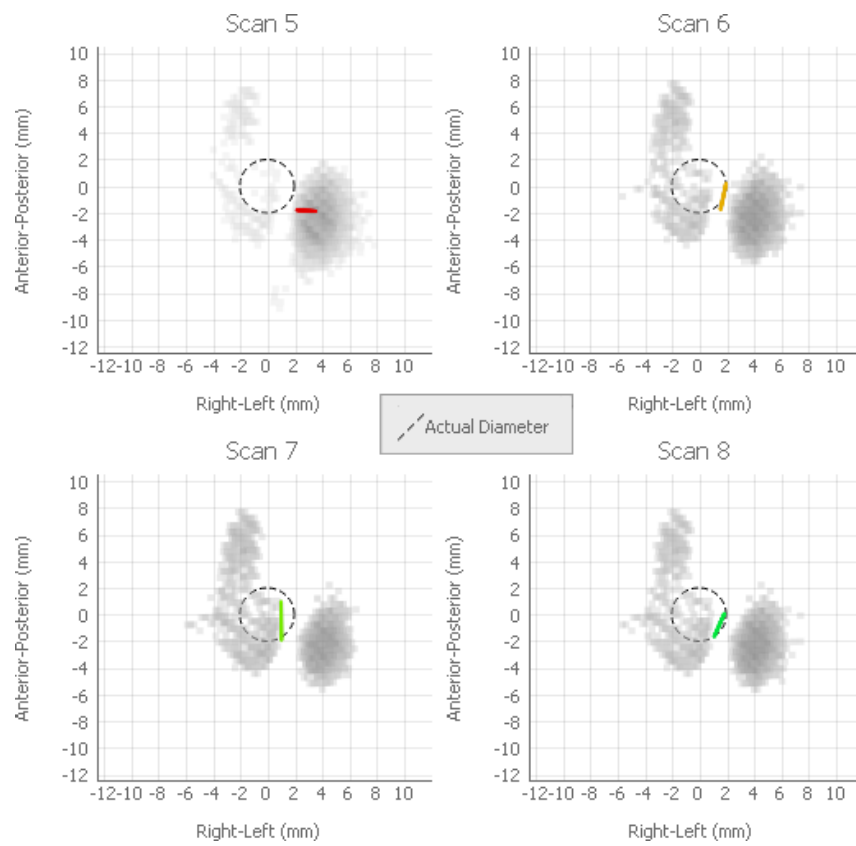
Figure 5.7: Line fitting results (coloured) and point-cloud data thresholded with $\Gamma = 0.21\%$ from scans 5-8 projected onto the needle axis.
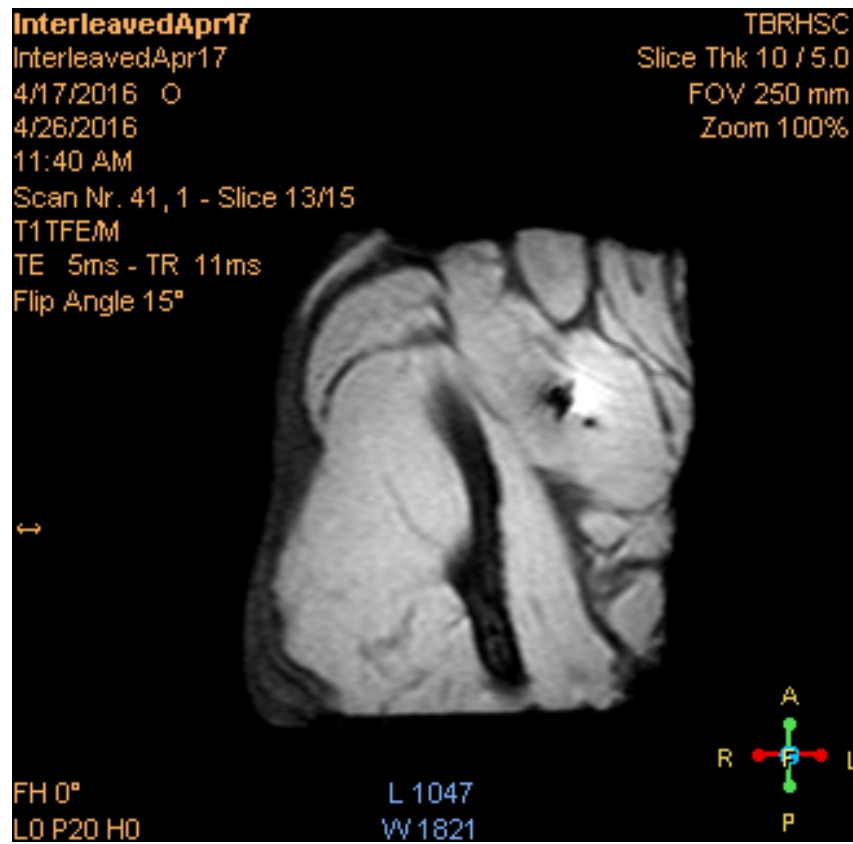
Figure 5.8: Verification scan transverse slice.

study. Mean skin to target time includes the time required for orientation scans. Pre-procedure imaging time includes the time required for initial scout images and planning/baseline image acquisition. Alignments are counted as the number of times scan planes are repositioned along the needle trajectory either before or during placement. Fig. 5.10 compares transverse cross sections of 3D orientation scan image data collected from 4 cm into the orientation scan field of view in the patient head direction. SNR measurements for the datasets of Fig. 5.10 (a) and Fig. 5.10 (b) are 150.9 and 29.81 respectively taken over ROIs surrounding the needle artifact.[1] SNR measurements for the datasets of Fig. 5.10 (c) and Fig. 5.10 (d) are 153.1 and 13.1 respectively taken over an ROI segmented with $\Gamma = 0.21\%$. Fig. 6.2 plots SAR measurements acquired across a orientation scan interleaved with visualization scans. SAR measurements were collected from SAR figure log messages posted to the scanner console General Information System and scaled according to SAR values reported in corresponding DICOM output. The max reported value for either visualization or orientation scan when run without interleaving is shown with a dashed line. $\frac{dB}{dT}$ measurements for orientation and visualization scans are taken from DICOM address [0018,1318] are 85.197 $\text{T} \cdot \text{s}^{-1}$ and 62.577 $\text{T} \cdot \text{s}^{-1}$ respectively. Noise levels during visualization scan acquisitions were measured to be between $99 - 101$ db(A), while noise levels during orientation scan acquisitions were measured to be between $98 - 100$ db(A). Noise levels were collected from behind the 5-gauss safety line at the edge of the scanner's fringe field with a VU meter (MRA Inc., Washington, PA). Fig. 5.9 shows an example of the localizer mechanism aligning the proposed configuration scan planes along the detected needle trajectory. Table 5.2 shows the targeting accuracy results for phantom and *ex-vivo* trials compared to results from similar fixed plane study [29]. Alignment accuracy results collected during time trial experiments as measured within visualization images are plotted in Fig. 5.11. A single outlying set of measurements resulted when the frame was accidentally displaced about 2 mm towards the patient right direction between orientation scans. The measurements plotted in Fig. 5.11 were used to calculate parameters for Eq. 2.9 and verify that the biopsy needle was entirely visualized after 93.8 % of alignments (i.e. in all cases except the aforementioned outlying result). The same calculations indicate that the average distance of the biopsy needle tip edge from the the slice boundary was

---

[1]Because there are insufficient "noise only" regions for use of the ROI method to compute these SNR values, noise standard deviation levels are estimated from the corresponding datasets of Fig. 5.10 (c) and Fig. 5.10 (d) and adjusted by a factor of $\sqrt{2}$.
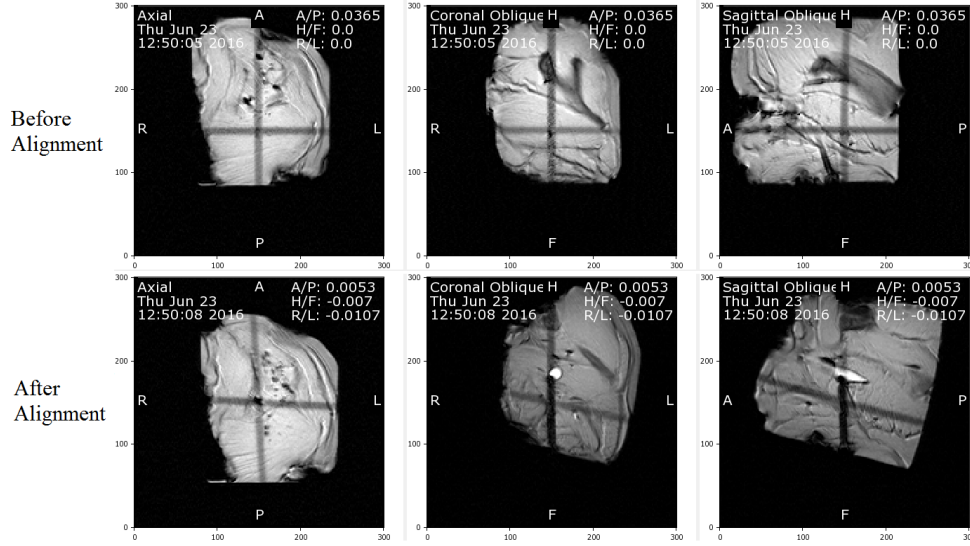
Figure 5.9: A comparison of screenshots showing scan plane alignment before and after the control mechanism is executed.

2.0 mm. Separately collected alignment results acquired at 1 cm increments of insertion length along two fixed trajectories of (a) 19.4° and (b) 9.8° from co-aligned static magnetic field and orientation scan frequency encoding axes are plotted in Fig. 5.12. All alignment results were calculated from visualization scans using Philips DICOM Viewer R3.0-SP03. Position error was determined based on the transverse plane images, longitudinal error determined on the basis of oblique coronal plane alignment and lateral error determined on the basis of oblique sagittal plane alignment.

Table 5.2: Targeting accuracy comparison between PCA-based alignment mechanism and a similar study using fixed scan planes.

	Mean targeting error (mm)		
	In-plane		
	x	y	Out-of-plane
PCA-based Mechanism Phantom	7.1(±3.5)	4.0(±1.9)	4.0(±3.26)
PCA-based Mechanism *Ex-vivo*	4.4(±0.5)	2.4(±1.1)	4.0(±0.8)
Rothgang *et al.* (2013) Phantom	1.6(±1.3)	2.2(±1.9)	1.9(±1.3)
Rothgang *et al.* (2013) In-vivo Kidney	3.4(±1.7)	2.5(±1.8)	2.2(±2.0)

Table 5.3: Procedure time comparison between PCA-based alignment mechanism and a similar fixed plane experiment.

Parameter	Time			
	PCA Phantom	PCA *Ex-vivo* Animal	[29] In-vivo Animal	[29] In-vivo Patient
Pre-procedure imaging time	66 sec	66 sec	70 sec	172 sec
Mean planning time	n\a	n\a	6 min $\pm$ 2 (5 needles)	4 min$\pm$ (4 needles)
Entry point localization time	n\a	n\a	< 60 sec	
Mean skin to target time	147 sec $\pm$ 32	269 sec $\pm$ 347	113 sec $\pm$ 57	76 sec $\pm$ 30
Verification imaging time	226 sec	226 sec	41 sec	23 sec
Alignments	1.3 $\pm$ 0.5	3.3 $\pm$ 1.2	1	1

(a)   (b)

(c)   (d)
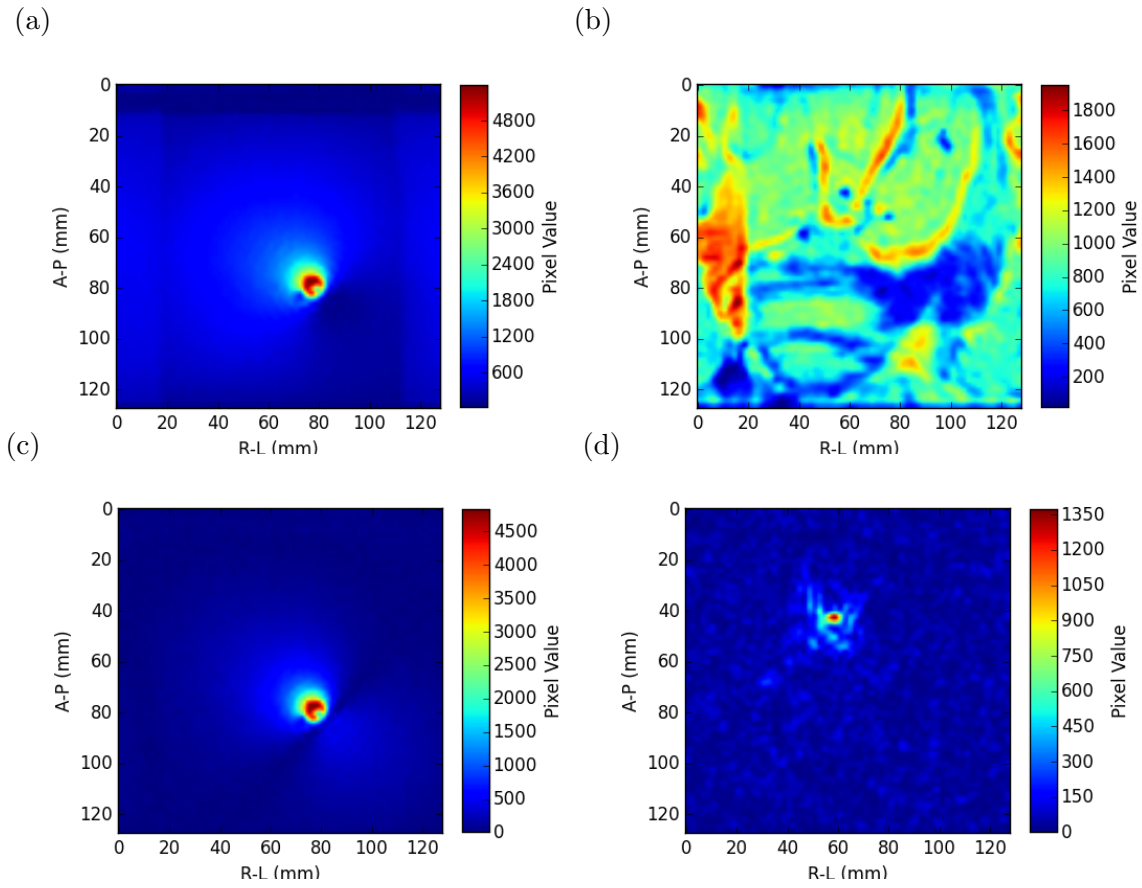
Figure 5.10: A comparison of transverse cross sections taken from orientation scan data: (a) phantom before baseline subtraction, (b) *ex-vivo* specimen before baseline subtraction, (c) phantom after baseline subtraction, (d) *ex-vivo* specimen after baseline subtraction.
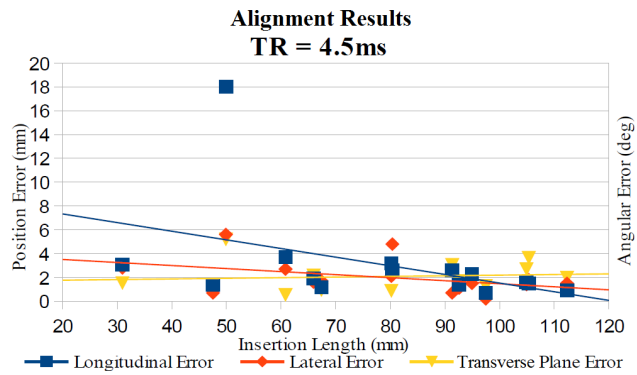
Figure 5.11: Alignment accuracy results collected during time trial experiments as measured within visualization images.
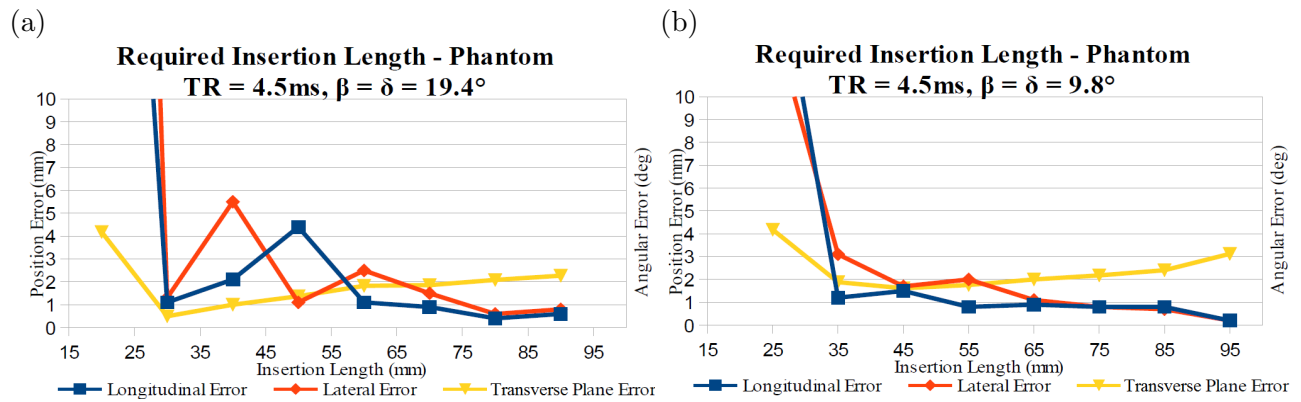
Figure 5.12: Alignment results plotted for a range of insertion lengths along an angle (a) 19.4° and (b) 9.8° from co-aligned static magnetic field and orientation scan frequency encoding axes.

Chapter 6

Discussion

.

6.1 Preliminary Effectiveness Study

The proposed algorithm achieves sub-millimeter and sub-degree accuracy in determining the position and orientation of a biopsy needle within tissue given the right scan and algorithm parameters as shown in Table 5.1. Selecting values for T_R resulting in SNR as low as 57.34 without any of the acceleration techniques described in Chapter 4 produced the desired result, however lower values may also produce an acceptable result at a reduced scan time provided they are beyond the previous data point. Fig. 5.2 shows two competing processes observed in choosing a threshold value for the initial segmentation of affected voxels: exclusion of noise voxels vs. exclusion of voxels located in the immediate vicinity of the device. The optimal value of Γ determined retrospectively in this study may serve as a reasonable guess for future experiments or one may be calculated based on the volume of the device contained within orientation scan field of view. The segmented number of points $m = 551$ corresponds to an equivalent cylindrical volume of 6.4 mm in diameter[1] suggesting that observations contribute to the orientation calculation within roughly 1.4 mm beyond the needle outer diameter. Results from accelerated scans (#5-#8) exhibited insufficient voxel isotropy to ensure symmetrical signal dephasing in the vicinity of the needle. All line fitting position errors shown in Fig. 5.6 and Fig. 5.7 are observed to tend toward signal pile-up effects exhibited along the frequency encoding direction of each scan according to the expected intensity profile of the needle susceptibility artifact [77]. Sig-

---

[1]Based on a needle length across the entire orientation scan field of view at an angle of $20°$.

nal dephasing surrounding this artifact is exacerbated in scans with minimal T_r values creating asymmetrical point-cloud projections in scans #1 and #5. Acceleration by parallel imaging with surface coils was not evaluated due to the implications for restricted access to the specimen. The heterogeneous distribution of muscle and fat in the vicinity of the needle appears to influence the segmentation pattern of voxels as projected in Fig. 5.6 and Fig. 5.7.

The minimum scan time required to achieve thesis objective #2 of 14.6 s provides an attractive alternative to manual scan plane adjustments or cumbersome device registration configurations which require much longer to prepare. Position error was not considered along the needle axis in this evaluation as rectilinear translation of the device along this axis is expected subsequent to localization. The technique could easily be extended to retrieve a second principal component to determine optimal double-oblique scan plane orientations for a curvilinear instrument or directional probe. Given the likelihood of organ/tissue deformation or involuntary patient motion, multiple baseline scans or motion artifact mitigation techniques such as respiratory/cardiac gating for orientation scan acquisition may be required during in-vivo studies. The computation time required to perform the proposed algorithm was observed to be roughly constant and considered insignificant relative to the total orientation scan acquisition time.

6.2   Feasibility Study

The automated scan plane alignment technique featured in this study has the potential for incorporation into a simplified workflow for an MR-guided needle intervention. The employed hardware and software modifications afforded volunteers intraprocedural adjustment of device trajectory to produce time and accuracy results comparable with those from a similar fixed plane study. The comparison is not meant to show that the workflow used in this work produces superior results than those of other studies but that it is technically feasible to achieve desirable outcomes using the new technique. In-plane targeting error of less than 5 mm is acceptable in most situations, and approximately this result was obtained from volunteers who were totally untrained in interventional radiology. Virtually no trajectory planning or entry point localization time was required as these were chosen arbitrarily during each volunteer attempt. Adequate imaging quality was attained from use the scanner body coil, maximizing volunteer access to the specimen. The verification imaging time was increased beyond that of the fixed plane study to ensure adequately small reconstruction voxel size without use of any acceleration techniques.

Volunteers were able to control scan plan alignment accurately with five degrees of freedom by pressing a single switch without use of their hands or necessarily deviating their eyes from the specimen or visualization screen. The required insertion length for useful scan plane alignment depended on the angle of insertion as measured from the static magnetic field and from the frequency encoding axes. At a double oblique trajectory of $\delta = \beta = 19.4°$, stable alignment results were obtained from insertion beyond 6 cm as seen in Fig. 5.12 (a). Short of this length, the needle artifact diameter was comparable to its length and consequently the direction of greatest variation among voxels affected by the needle was a less effective indication of true needle orientation. Between 3 cm and 6 cm of insertion length, the centroid calculation was most accurate and partial visualization was still possible. Beyond 6 cm, results converge on those observed in §5.1 for full insertion across the 12.8 cm orientation scan field of view using the same scan parameters and approximately the same insertion angle. For an oblique trajectory such as this, dephasing and spatial distortion effects are not symmetrical about the needle axis according to the passive visualization model discussed in §2.2. The diameter of these asymmetrical effects tapers towards the tip of the needle where the tip geometry disrupts the continuity of distortion effects. Consequently, displacement error in the transverse plane increases with the inserted length of the needle, however angular error decreases due to the parallel formation of the artifact regardless of diameter.

Eq. 2.1 holds for voxels where transverse magnetization is naturally spoiled to the extent that the voxel has been segmented along with those corresponding to the needle signal void itself. Consequently Fig. 5.12 (b) shows reduced angular error with a trajectory more closely aligned with both $\mathbf{B_0}$ and $\mathbf{G}_f$. Angular error in this case is stabilized at an insertion length of about 3.5 cm.

6.2.1 Artifacts

Fig. 6.1(a) shows the effect of aliasing on orientation scan image data across a transverse cross-sectional image. The needle susceptibility artifact has been intentionally dilated by insertion of an aluminum rod into the needle lumen to enhance the effect. The presence of the biopsy needle (oriented primarily in the head-foot direction) is erroneously localized on the right side (patient left) of the image space to the extent that it passes beyond the left hand (patient right) boundary of the orientation scan field of view. This is an inherent consequence of eliminating
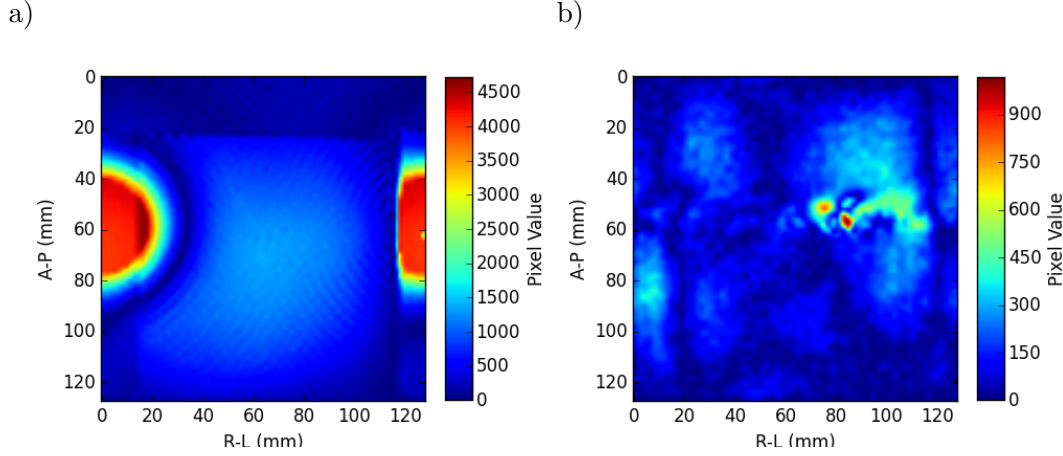
Figure 6.1: Transverse slices of orientation scan data showing the effects common artifacts on detection of a biopsy needle: (a) aliasing of a dilated needle artifact extending beyond the left side (patient right) of the FOV, (b) motion artifact around a needle which was withdrawn from the slice volume during acquisition.

oversampling in phase encoding directions for orientation scan acquisitions to minimize scan time. The reach of the fold-over is seen to be truncated by the specimen tissue boundary. This artifact completely corrupts the localization results of Algorithm 1 according to Eq. 4.4 where factor scores of aliased voxels are offset by a distance equal to the scan FOV. Only aliased tissue which experiences a change in signal magnitude between scans contributes to this problem. In other words, erroneous results caused by aliasing artifact can be avoided if interventional device placement is restricted so that the device susceptibility artifact does not extend beyond the orientation scan FOV. Resizing orientation scan FOV settings to enclose the actual subject tissue dimensions while the acquisition matrix size remains fixed will preclude the possibility of this artifact occurring at the cost of lost precision along the dimensions for which the voxel size has been increased. Spatial presaturation pulses can be added to an orientation scan imaging sequence to preemptively excite and dephase signal contribution from the extraneous tissue regions which could allow fold-over to occur [18].

Fig. 6.1 (b) shows the effect of motion artifact in orientation scan image data in the case a biopsy needle withdrawn 1.8 cm along the needle axis during scan acquisition. As described in §2.4.1, motion artifact appears across directions along which spatial encoding iterates over a sufficiently long period for voxel signal amplitudes to be modulated. Here, ripples of motion
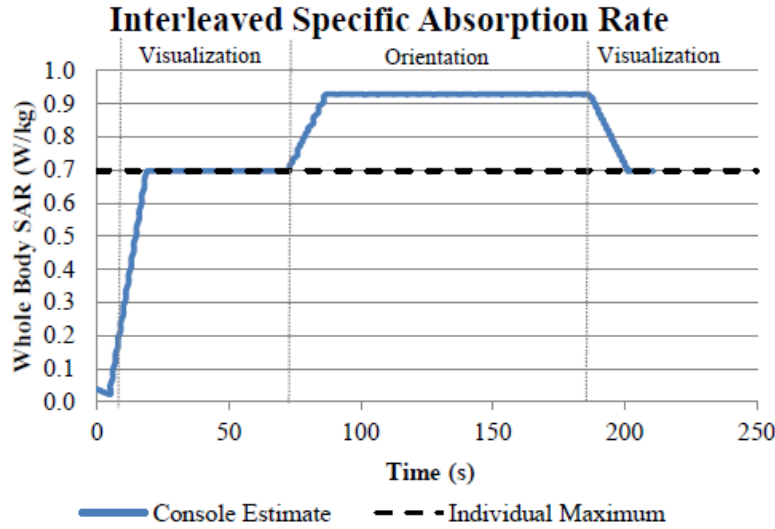
Figure 6.2: SAR values plotted over a sequence of scans.

artifact span the image space horizontally as the right-left direction was configured for the outer iteration of phase encoding which takes place over periods of $N_z \cdot N_y \cdot T_R$ as opposed to $N_y \cdot T_R$ only for the inner iterations corresponding to the vertical (anterior-posterior) direction. The resulting localization was shifted by 4.0 mm towards the patient right direction versus only 0.2 mm towards the posterior direction, as well as 6.53° longitudinally versus only 4.18° laterally.

6.2.2 SAR Estimates

Whole body SAR values plotted within Fig.6.2 are well within allowable values specified in Table 2.2. Interestingly, SAR is reported to increase by up to 33% when scans are interleaved in the manner proposed in §4.3. As mentioned, the Philips model for calculating these estimates is proprietary and serve as a worst case prediction. The cause of this observed increase is unclear however it is evident that the Philips SAR model expects delivery of RF energy to be compounded by rapid interleaving of these two scans. This may become a relevant consideration should the scan plane alignment technique of this work be employed with spin echo sequences where increased scan times are required to compensate for increased SAR delivery.

6.2.3 Peripheral Nerve Stimulation

Philips MR release 3.2.3. prompts a 'potential peripheral nerve stimulation' warning based on the $\frac{dB}{dt}$ value of $85.197 \, \text{T} \cdot \text{s}^{-1}$ for orientation scans reported in §5.2. This warning corresponds to the IEC first level controlled operating mode limit for time varying magnetic fields implying
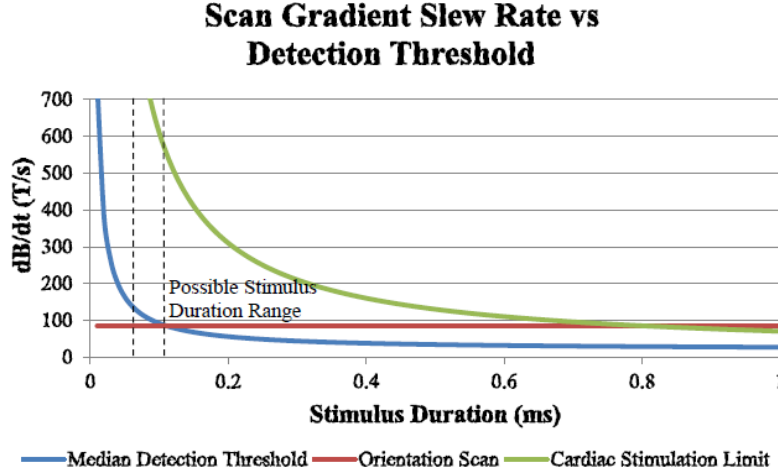
Figure 6.3: The range of possible stimulation duration corresponding to first level controlled operating mode for the given $\frac{dB}{dt}$ value reported for orientation scans.

gradient $\frac{dB}{dt}$ is between 80% to 100% of median detection threshold values determined from Eq. 2.21. Although exact stimulus duration (Ω) values are not provided from the MR console, the corresponding range of possible values from 0.083 ms to 0.110 ms is noted in Fig. 6.3. These durations provide a large margin of safety between the reported $\frac{dB}{dt}$ value and the corresponding IEC cardiac stimulation limits determined from Eq. 2.22 as 555.5 T·s^{-1} to 732.9 T·s^{-1}. MR scanners are configured to limit gradients according to IEC requirements, however nerve stimulation has been recorded under the same conditions and even at lower values of time varying magnetic field [78]. This result may pose implications for employment of orientation scans as described in Chapter 4. MR examinations must be halted once PNS occurs [1]. A clinicians motor control may be affected without warning should their peripheral nerves be stimulated while manipulating interventional instrument, however instrument motion is not advised during orientation scan acquisition to avoid motion artifact generation.

6.3   Noise

Noise levels measured during orientation scan acquisition are measured to be about the same as during visualization scans and are consistent with values reviewed in §2.6.3. This confirms that there is no added noise safety hazard posed to a scanner operator during employment of the orientation scan alignment technique. This rhythm is clearly audible through both levels of hearing protection (NRR ∼ 63). The rhythm of noise emitted from the scanner during orientation

scan acquisition is distinct from that of visualization scans giving feedback to the operator about exactly when the orientation scan is initiated and when the visualization scans have resumed. The rhythm of audible noise during visualization scans likewise allows the operator to adjust their hand motions for the effective latency of visualization images presented after their acquisition is complete.

6.4 Comparison With Other Solutions

Marketing material for GE MR echo and HeartVista Inc. RTHawk show scan plane alignment changes taking effect within seconds using a 'drop-line' tool for perpendicular slice navigation though use of hands is required [79, 80]. A study on pulse sequence switching with GE iDrive interface using a 1.5T Signa Excite timed an operator switching quickly between two sequences for a mean of up to 28 seconds over three attempts without having to actually modify any parameters. In the same manner, an MR Technologist was timed at the Philips Achieva 3.0 T running Philips MR to arrange a multi-stack configuration of scan planes in the same relative orientation as described in §4.3 along arbitrary double oblique orientations. The mean over three attempts was $T_m = 140.9$ s. The measured technologist manual alignment time can be extrapolated according to Fig. 1.1 where each iteration of manual alignment requires a restart of the scanner with prerequisite shimming process as well as scout images requiring an additional $T_s = 38$ s. An estimate of the net time savings acquired during the phantom and *ex-vivo* studies is calculated to be 213.85 sec and 582.85 sec respectively according to the following expression:

$$(T_\mathrm{S} + T_\mathrm{m} - T_c) \times a \tag{6.1}$$

where a is the average number of alignments performed taken from Table 5.3 and T_c is the time required to employ the scan alignment mechanism calculated in Eq. 4.15. The average total time for needle placement was 213 sec and 335 sec for phantom and *ex-vivo* trials respectively.

6.5 Limitations

The orientation scan alignment technique described in this technique does not fully address two aspects of device placement which are significant considerations for incorporation into interventional workflows: motion and device tip localization.

6.5.1 Motion

As discussed in §2.4.1, tissue motion that modulates signal amplitude *during* orientation scan acquisition creates artifacts across the phase encoding directions of the image space. For a 3D orientation scan with two dimensions of phase encoding which are perpendicular to the static magnetic field, this artifact is manifested as transverse planes of erroneous magnitude information which intersect the affected voxels. This effect would be particularly detrimental to the PCA calculations employed in this work where noisy pixels would not necessarily be localized in close proximity to the actual trajectory and contribute disproportionately to the calculation of principal component according to Eq. 4.4. During feasibility study experiments, volunteers were instructed not to reposition the biopsy needle during orientation scan acquisition. Additional sources of tissue motion could include periodic respiratory or cardiac motion as well as aperiodic patient movement.

Because image magnitude values are subtracted from a baseline, any change in voxel signal magnitude *between* orientation scans will also have an effect on the localization results. This effect is restricted to the regions in which the signal magnitude change has occurred including deformation of organs or tissue around the device trajectory. Other signal magnitude changes that occur during or between orientation scans aside from those directly generated by the placement of a device would most likely result from some form of involuntary tissue motion but also possibly from image artifacts such as cross-talk from preceding acquisitions in a time-interleaved scan protocol. For example, the multislice visualization images employed in this work are themselves interleaved within their acquisition independently from the time-interleaving settings of Table 4.5. This can potentially result in regions of reduced signal level within subsequent orientation scan image data which could register as motion upon subtraction of this data from a baseline dataset. There is a wide variety of motion compensation techniques can be employed to deal with the problem of motion in MR [31]. Respiratory or cardiac gating can be utilized to collect signal in small increments in sync with periodic motion at an increased overall scan duration. One dimensional navigator acquisitions can be interleaved amongst visualization scans to track periodic motion cycles as part of a multi-baseline motion correction approach [81]. This technique could be adapted such that subtraction of orientation scan data could be calculated in reference to the most appropriate baseline dataset within a look-up table corresponding to different

phases of the motion cycle. The effects of aperiodic motion could be remediated by other signal conditioning techniques in addition to segmentation by thresholding as used in this work. Such strict thresholding ($\Gamma \sim 0.2\%$) relies on an assumption that the greatest contrast in an image dataset occurs between tissue (ideally ρ-weighted) and the signal void created by the presence of a titanium needle. However, additional clusters of voxel position vectors may be erroneously included by this technique in the case of independently moving organs. K-means clustering [82] could be used to iteratively group point clouds around their respective centroids and the cluster most closely corresponding to the device position automatically determined based on a priori knowledge of the expected device trajectory.

6.5.2 Needle Tip Localization

Although the centroid position ($\bar{\mathbf{s}}$) calculated with Algorithm 1 localizes the centre of a biopsy needle artifact along the needle axis, one of the most critical aspects of biopsy needle placement is tracking the needle tip. Setting a visualization scan FOV wider than the insertion length of the needle ensures complete visualization of the tip provided scan plane alignment is adequate. In this approach, proper placement of the needle tip is left up to an interventionalist and confirmed manually with verification scans. Assumptions about the tip position relative to the calculated centroid location are problematic as the contrast of surrounding tissues along the length of the needle is potentially non-uniform. Needle tip bloom artifact and partial volume effects complicate matters further by obscuring representation of the tip end. Fig. 6.4 (a) shows that the signal void of the needle is well pronounced at a point along the length of the needle, however bloom dephasing affect voxel signal magnitudes less starkly around the tip as shown in Fig. 6.4 (b) and ahead of the tip shown in Fig. 6.4 (c), thus localization towards the needle end point becomes difficult. In light of these challenges, the position accuracy results of §5.1 have been limited error calculations to orthogonal distance from the true needle axis. Negative contrast from passive susceptibility markers shown in Fig. 4.1 are an example of visualization features built into a device that may help with tip localization. Despite the drawbacks of active tracking techniques discussed in §3.1, the positive contrast of resonant markers fixed on the needle at distances relative to the tip would produce image datasets compatible with Algorithm 1.
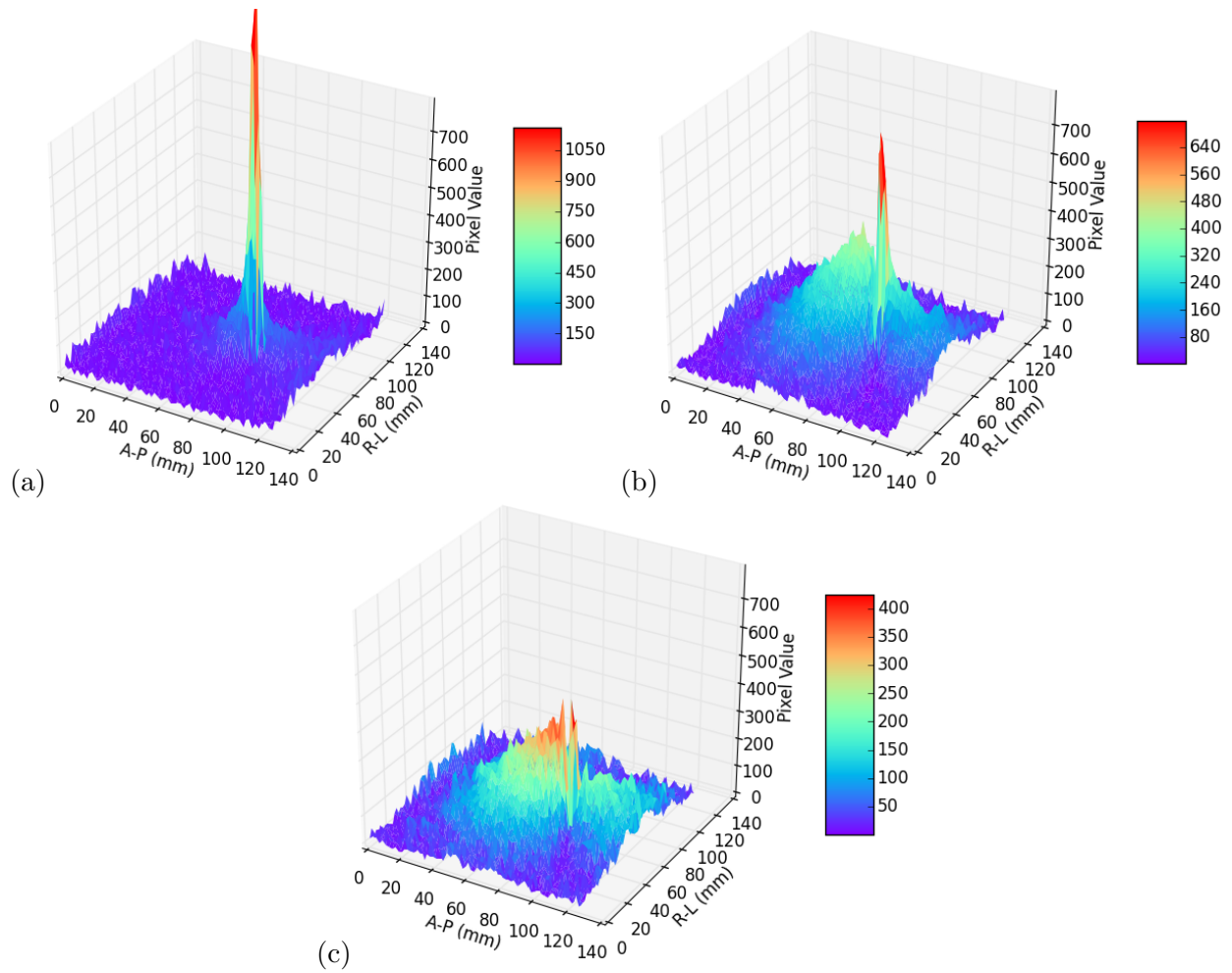
Figure 6.4: Comparison of surface plots for orientation scan image data transverse cross sections at (a) a midpoint of the biopsy needle showing signal void, (b) needle tip with surrounding bloom artifact and (c) bloom and dephasing artifact 2 mm ahead of the needle tip.

Chapter 7

Conclusion

This chapter provides brief conclusions about the achievements of the work with respect to the objectives outlined in §1.3, along with recommendations for potential applications of the developed system are discussed.

7.1 Achievements of This Work

An MR image-based localization mechanism has been presented to determine the position and alignment of a linearly shaped interventional device entirely from 3D MRI orientation scan image data and visualize the device accordingly to satisfy Objective #1. The performance of the localization algorithm was demonstrated over a range of scanning parameters to be adequate for potential applications such as dynamic scan plane alignment for MR-guided interventions or placement verification for MR-guided prospective stereotaxy. With respect to Objective #2, device localization was adequate to contain a biopsy needle within a visualization slice volume after 93.8% of alignments over insertion lengths between 30 mm to 110 mm at insertion angles between 1.4° to 20° from the static magnetic field and frequency encoding axes. The algorithm was incorporated into a biopsy needle tracking system implemented with an MR-scanner operated by a footswitch only to satisfy Objectives #3 and #4. Time trials produced a mean targeting error across all directions was 3.6 mm for the phantom trials and 5.1 mm for the *ex-vivo* trials respectively. The average entry to target time was 247 sec.

7.2 Future Work

The technique proposed in this work shows potential for incorporation into existing interventional workflows to yield reduced procedure times, increase the sensitivity of biopsy results and otherwise increase the accuracy of interventional device placement. An in-vivo study is required to assess the tolerance of the proposed method under conditions of patient motion. Although designed for biopsy needle artifacts as a representative interventional device, this system can potentially operate with any phenomena which can be segmented from image data such as thermometry mapping, acoustic radiation force imaging (ARFI), or contrast-enhanced MR-angiography(CE-MRA). Only a change of input data is required to begin experimenting with these imaging techniques and calculating the optimal visualization there-of.

Appendices

Appendix A

A.1 Description of Specialized Interventional Scanner Units

Major diagnostic imaging device vendors (GE Healthcare, Siemens Healthcare, Philips Healthcare, Toshiba Medical Systems Corporation) provide solutions for interventional image guidance including specially designed scanner units. The GE Signa SP offers an upright 'double donut' scanner configuration providing clinicians with direct access to patients through a 58 cm horizontal gap between segmented 60 cm diameter bore sections. The separate static field magnets and gradient coils are positioned to remotely influence a 30 cm diameter imaging volume at 0.5 T static field strength, $12 \text{ T} \cdot (\text{m} \cdot \text{s})^{-1}$ slew rate and $12 \text{ mT} \cdot \text{m}^{-1}$ gradient field strength [1]. Entirely open bore scanners such as the Philips Panaroma HFO gives broad patient access between two 160 cm diameter magnets, set 40 cm apart vertically to produce a vertical magnetic field of 1.0 T, a slew rate of $80 \text{ T} \cdot (\text{m} \cdot \text{s})^{-1}$ and a $26 \text{ mT} \cdot \text{m}^{-1}$ gradient field strength [83]. Wide bore diameter scanners are available in $3 \, T$ field strengths such as the Toshiba Vantage Titan 3.0 T with a 70 cm diameter bore, slew rate of $170 \text{ T} \cdot (\text{m} \cdot \text{s})^{-1}$ and gradient field strength of $33 \text{ mT} \cdot \text{m}^{-1}$. [84, 85]. Finally, short bore scanners improve patient access over closed bore diagnostic units due to their reduced length in the head-foot direction such as 125 cm for the Siemens Magnetom Espree with field strength of 1.5 T, slew rate of $170 \text{ T} \cdot (\text{m} \cdot \text{s})^{-1}$ and gradient field strength of $33 \text{ mT} \cdot \text{m}^{-1}$. The aforementioned specialized scanner installations are discussed in the context of having a surgical environment co-located with a scanner environment, however other intra-operative suite designs are possible.[1] The IMRIS Visius iMRI surgical theater commissions a

---

[1]The term 'intra-operative MRI (iMRI)' is often used in literature synonymously with real-time imaging as is used in this work, however the term can also entail 'in-and-out' imaging where the patient is temporarily moved outside of the scanner bore during device placement.

Siemens 3.0 T movable magnet scanner with slew rate of 200 T $\cdot$ (m $\cdot$ s)$^{-1}$ and gradient strength of 45 mT $\cdot$ m^{-1} on a sliding ceiling mount and can be removed from around the patient table during device placement [86]. Movable patient positioning systems are also available to transfer patients between imaging and surgical environments located in the same or adjoining rooms to facilitate the intra-operative imaging process [87].

A.2 Additional Background for Principal Component Analysis

Principal Component Analysis (PCA) is a widely used tool for statistical analysis of multivariate data in which linearly independent factors (principal components) are calculated as a basis upon which observed data can be projected to exhibit the greatest variation [64]. These components consist of linear combinations of the original variables and exhibit orthogonality. PCA is useful for dimension reduction where the principal components which span the least variation amongst variables may be discarded to create a useful representation for visualization or comparison of observations. The PCA concept is summarized as follows.

- Collect n p-variable observations $\mathbf{R} = (\mathbf{r}^{(1)}, \mathbf{r}^{(2)}, \dots, \mathbf{r}^{(n)})$.

- Determine the vector $\hat{\mathbf{u}}^{(1)}$ along which the greatest variation of observation data occurs to be the first principal component in order of significance.

- Repeat the previous step subject to constraint of orthogonality $p - 1$ times until only one vector $\hat{\mathbf{u}}^{(p)}$ remains as the last principal component in order of significance.

- Project data $\mathbf{R}$ onto principal components with a linear transformation $\mathbf{U} = (\hat{\mathbf{u}}^{(1)}, \dots, \hat{\mathbf{u}}^{(p)})$.

- Discard least significant elements of each observation as is justified to create a variable-reduced approximation of data.

Determining a unit vector $\hat{\mathbf{v}}$ representing the direction of greatest variation is a problem of maximizing the variance of projections, also called factor scores, onto an axis parallel to $\hat{\mathbf{v}}$ by mean-centered observations [88]. The variance of these projections can be described by:

$$\frac{1}{n-1} \sum_{i=1}^{n} \left(\mathbf{r}^{(i)^T} \hat{\mathbf{v}} \right)^2 = \frac{1}{n-1} \sum_{i=1}^{n} \hat{\mathbf{v}}^T \mathbf{r}^{(i)} \mathbf{r}^{(i)^T} \hat{\mathbf{v}} \tag{A.1}$$

$$= \hat{\mathbf{v}}^T \left(\frac{1}{n-1} \sum_{i=1}^{n} \mathbf{r}^{(i)} \mathbf{r}^{(i)^T} \right) \hat{\mathbf{v}} \tag{A.2}$$
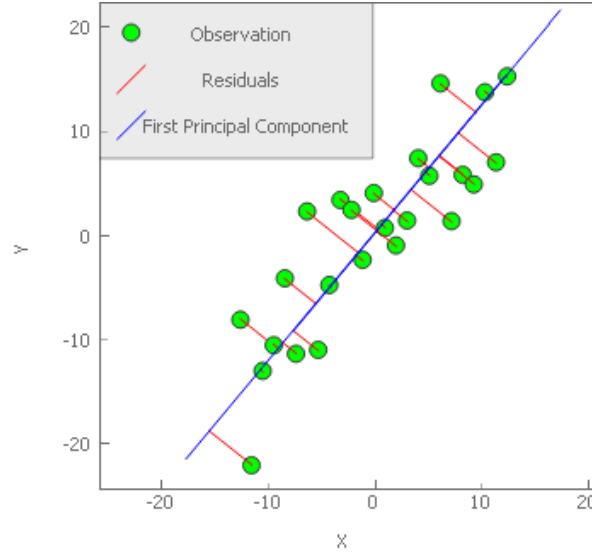
Figure A.1: A graphical example of a principal component analysis result based on independent variables x and y.

$$= \hat{\mathbf{v}}^T (\mathbf{C}) \hat{\mathbf{v}} \tag{A.3}$$

$\mathbf{C} = \left(\frac{1}{n-1} \sum_{i=1}^{n} \mathbf{r}^{(i)} \mathbf{r}^{(i)^T} \right)$ is an empirical covariance matrix which yields eigenvector matrix of principal components $\mathbf{U} = (\hat{\mathbf{u}}^{(1)}, \dots, \hat{\mathbf{u}}^{(p)})$ with associated eigenvalues $\boldsymbol{\lambda} = (\lambda_1, \dots, \lambda_d)$ in order of size by singular value decomposition [65]. Because $\hat{\mathbf{v}}$ is subject to the constraint $||\hat{\mathbf{v}}||^2 = 1$, the maximum variance is obtained from selecting $\hat{\mathbf{v}}$ as $\hat{\mathbf{u}}^{(1)}$, the first principal component vector.

The orthogonal distance from each observation onto the first principal component axis $\mathbf{r}^{(i)} - \left(\mathbf{r}^{(i)^T} \hat{\mathbf{u}}^{(1)} \right) \hat{\mathbf{u}}^{(1)}$ (called a residual) is a composite of remaining principal component vectors $(\hat{\mathbf{u}}^{(2)}, \dots, \hat{\mathbf{u}}^{(p)})$ and is minimized across all observations as illustrated in Fig. A.1). This outcome of principal component analysis is desirable for calculating a line of best fit from isotropic orientation scan data as error is assumed to exist in all dimensions of observation data unlike least-squares linear regression techniques [89]. The contribution $\psi_{i,j}$ of the i-th factor score f to the calculation of component j with associated eigenvalue λ_j is given by:

$$\psi_{i,j} = \frac{f_{i,j}^2}{\sum_{k}^{n} f_{k,j}^2} = \frac{f_{i,j}^2}{\lambda_j} \tag{A.4}$$

where $f_{i,j} = \left(\hat{\mathbf{u}}^{(j)} \right)^T \mathbf{r}^{(i)}$ and $\lambda_j = \sum_{k}^{n} f_{k,j}^2$. Eq. A.4 shows an important characteristic of PCA, it is sensitive to the presence of outliers amongst observations. As an observation is moved further

from the mean in terms of factor score, its contribution to a corresponding principal component is squared [69].

The computational complexity of completing a principal component analysis is dominated by the covariance matrix calculation with $O(np^2)$ [67] where n is the number of observations and p is the observation vector dimensionality. Subsequent calculation of eigenvectors as principal component vectors from the covariance matrix comes with an additional computational cost as high as $O(p^3)$ [90]. The combined computation cost is given in Eq. A.5.

$$O(np^2 + p^3) \approx O(n), \quad n \gg p \tag{A.5}$$

Bibliography

[1] Thomas Kahn and Harald Busse. *Interventional Magnetic Resonance Imaging.* Springer, 2012.

[2] Clare M Tempany. *MR-Guided Interventions, An Issue of Magnetic Resonance Imaging Clinics of North America 23-4*, volume 23. Elsevier Health Sciences, 2016.

[3] Jonathan Scalera, Xinyang Liu, Gary P Zientara, and Kemal Tuncali. From subjective to objective: Quantitative computerized monitoring tool for mri-guided cryoablation. In *Workshop on Clinical Image-Based Procedures*, pages 88–95. Springer, 2015.

[4] William Chu, Robert M Staruch, Samuel Pichardo, Matti Tillander, Max O Köhler, Yuexi Huang, Mika Ylihautala, Merrylee McGuffin, Gregory Czarnota, and Kullervo Hynynen. Magnetic resonance-guided high intensity focused ultrasound hyperthermia for recurrent rectal cancer: Mr thermometry evaluation and preclinical validation. *International Journal of Radiation Oncology* Biology* Physics*, 2016.

[5] Kanishka Ratnayaka, Toby Rogers, William H Schenke, Jonathan R Mazal, Marcus Y Chen, Merdim Sonmez, Michael S Hansen, Ozgur Kocaturk, Anthony Z Faranesh, and Robert J Lederman. Magnetic resonance imaging–guided transcatheter cavopulmonary shunt. *JACC: Cardiovascular Interventions*, 9(9):959–970, 2016.

[6] Sylvain Terraz, Rares Salomir, and Christoph D Becker. Mr-guided radiofrequency ablation of liver tumours. In *Intraoperative Imaging and Image-Guided Therapy*, pages 799–816. Springer, 2014.

[7] Aytekin Oto, Ila Sethi, Gregory Karczmar, Roger McNichols, Marko K. Ivancevic, Walter M. Stadler, Sydeaka Watson, and Scott Eggener. Mr imagingguided focal laser ablation for prostate cancer: Phase i trial. *Radiology*, 267(3):932–940, 2013.

[8] Elena A Kaye, Kristin L Granlund, Elizabeth A Morris, Majid Maybody, and Stephen B Solomon. Closed-bore interventional mri: Percutaneous biopsies and ablations. *American Journal of Roentgenology*, 205(4):W400–W410, 2015.

[9] Ned H. Kalin, Andrew S. Fox, Rothem Kovner, Marissa K. Riedel, Eva M. Fekete, Patrick H. Roseboom, Do P.M. Tromp, Benjamin P. Grabow, Miles E. Olsen, Ethan K. Brodsky, Daniel R. McFarlin, Andrew L. Alexander, Marina E. Emborg, Walter F. Block, Julie L. Fudge, and Jonathan A. Oler. Overexpressing corticotropin-releasing factor in the primate amygdala increases anxious temperament and alters its neural circuit. *Biological Psychiatry*, 80(5):345 – 355, 2016.

[10] Toby Rogers, Kanishka Ratnayaka, Parag Karmarkar, William Schenke, Jonathan R Mazal, Adrienne E Campbell-Washburn, Ozgur Kocaturk, Anthony Z Faranesh, and Robert J Lederman. Real-time magnetic resonance imaging guidance improves the yield of endomyocardial biopsy. *Journal of Cardiovascular Magnetic Resonance*, 18(1):376–383, 2016.

[11] Georgia Tsoumakidou, Guillaume Koch, Jean Caudrelier, Julien Garnon, Roberto Luigi Cazzato, Faramarz Edalat, and Afshin Gangi. Image-guided spinal ablation: A review. *CardioVascular and Interventional Radiology*, 39(9):1229–1238, 2016.

[12] Martin A Rube, Andrew B Holbrook, Benjamin F Cox, Razvan Buciuc, and Andreas Melzer. Wireless mobile technology to improve workflow and feasibility of mr-guided percutaneous interventions. *International journal of computer assisted radiology and surgery*, 10(5):665–676, 2015.

[13] Daniel R Elgort, Eddy Y Wong, Claudia M Hillenbrand, Frank K Wacker, Jonathan S Lewin, and Jeffrey L Duerk. Real-time catheter tracking and adaptive imaging. *Journal of Magnetic Resonance Imaging*, 18(5):621–626, 2003.

[14] Yong-Lae Park, Santhi Elayaperumal, Bruce Daniel, Seok Chang Ryu, Mihye Shin, Joan Savall, Richard J Black, Behzad Moslehi, and Mark R Cutkosky. Real-time estimation of

3-d needle shape and deflection for mri-guided interventions. *Mechatronics, IEEE/ASME Transactions on*, 15(6):906–915, 2010.

[15] Santhi Elayaperumal, Juan Camilo Plata, Andrew B Holbrook, Yong-Lae Park, Kim Butts Pauly, Bruce L Daniel, and Mark R Cutkosky. Autonomous real-time interventional scan plane control with a 3-d shape-sensing needle. *Medical Imaging, IEEE Transactions on*, 33(11):2128–2139, 2014.

[16] Robert W Brown, Y-C Norman Cheng, E Mark Haacke, Michael R Thompson, and Ramesh Venkatesan. *Magnetic Resonance Imaging: Physical Principles and Sequence Design*. John Wiley & Sons, 2014.

[17] Michael L Lipton. *Totally accessible MRI: a user's guide to principles, technology, and applications*. Springer Science & Business Media, 2010.

[18] Brian M Dale, Mark A Brown, and Richard C Semelka. *MRI: Basic Principles and Applications*. John Wiley & Sons, 2015.

[19] Mark E Ladd, Peter Erhart, Jörg F Debatin, Benjamin J Romanowski, Peter Boesiger, and Graeme C McKinnon. Biopsy needle susceptibility artifacts. *Magnetic resonance in medicine*, 36(4):646–651, 1996.

[20] Bernd Müller-Bierl, Hansjörg Graf, Ulrike Lauer, Günter Steidle, and Fritz Schick. Numerical modeling of needle tip artifacts in mr gradient echo imaging. *Medical physics*, 31(3):579–587, 2004.

[21] Haiying Liu, Walter A Hall, Alastair J Martin, and Charles L Truwit. Biopsy needle tip artifact in mr-guided neurosurgery. *Journal of Magnetic Resonance Imaging*, 13(1):16–22, 2001.

[22] Hákon Gudbjartsson and Samuel Patz. The rician distribution of noisy mri data. *Magnetic resonance in medicine*, 34(6):910–914, 1995.

[23] Albert Macovski. Noise in mri. *Magnetic Resonance in Medicine*, 36(3):494–497, 1996.

[24] Kevin M. Koch. K-space ismrm educational course, physics and techniques for clinicians. ISMRM 19th Annual Meeting and Exhibition, Montreal, Canada, 2011.

[25] Mark Hedley, Hong Yan, and Dov Rosenfeld. Motion artifact correction in mri using generalized projections. *Medical Imaging, IEEE Transactions on*, 10(1):40–46, 1991.

[26] G Menegaz. 2d discrete fourier transform (dft).

[27] Stephen R Yutzy and Jeffrey L Duerk. Pulse sequences and system interfaces for interventional and real-time mri. *Journal of Magnetic Resonance Imaging*, 27(2):267–275, 2008.

[28] Iulius Dragonu, Baudouin Denis de Senneville, Bruno Quesson, Chrit Moonen, and Mario Ries. Real-time geometric distortion correction for interventional imaging with echo-planar imaging (epi). *Magnetic resonance in medicine*, 61(4):994–1000, 2009.

[29] Eva Rothgang, Wesley D Gilson, Frank Wacker, Joachim Hornegger, Christine H Lorenz, and Clifford R Weiss. Rapid freehand mr-guided percutaneous needle interventions: An image-based approach to improve workflow and feasibility. *Journal of Magnetic Resonance Imaging*, 37(5):1202–1212, 2013.

[30] Richard Held and Nathaniel Durlach. Telepresence, time delay and adaptation. *Pictorial communication in virtual and real environments*, pages 232–246, 1991.

[31] Matt A Bernstein, Kevin F King, and Xiaohong Joe Zhou. *Handbook of MRI pulse sequences*. Elsevier, 2004.

[32] Brian Hargreaves. Fast gradient echo sequences including balanced ssfp. *Journal of Magnetic Resonance Imaging*, 20:857–864, 2004.

[33] Brian A Hargreaves, Pauline W Worters, Kim Butts Pauly, John M Pauly, Kevin M Koch, and Garry E Gold. Metal-induced artifacts in mri. *American journal of roentgenology*, 197(3):547–555, 2011.

[34] Paul Glover. Magnetic field-induced vertigo in the mri environment. *Current Radiology Reports*, 3(8):1–7, 2015.

[35] Jill K Bradley, Matilda Nyekiova, David L Price, Lindsay Lopez, and Therese Crawley. Occupational exposure to static and time-varying gradient magnetic fields in mr units. *Journal of Magnetic Resonance Imaging*, 26(5):1204–1209, 2007.

[36] Sami Kännälä, Tim Toivo, Tommi Alanko, and Kari Jokela. Occupational exposure measurements of static and pulsed gradient magnetic fields in the vicinity of mri scanners. *Physics in medicine and biology*, 54(7):2243, 2009.

[37] International Electrotechnical Commission. Iec 60601-2-33. *Medical Electrical Equipment-Part*, 2, 2010.

[38] Michael E Moseley, Chunlei Liu, Sandra Rodriguez, and Thomas Brosnan. Advances in magnetic resonance neuroimaging. *Neurologic clinics*, 27(1):1–19, 2009.

[39] L Zaremba and R Phillips. Fda guidelines for magnetic resonance equipment safety. In *Medical Physics*, volume 29, pages 1302–1303. Amer Assoc Physicists Medicine Amer Inst Physics ste 1 no 1, 2 Huntington Quadrangle, Melville, NY 11747-4502 USA, 2002.

[40] AbdEl-Monem M El-Sharkawy, Di Qian, Paul A Bottomley, and William A Edelstein. A multichannel, real-time mri rf power monitor for independent sar determination. *Medical physics*, 39(5):2334–2341, 2012.

[41] FG Shellock, M Ziarati, D Atkinson, and D-Y Chen. Determination of gradient magnetic field-induced acoustic noise associated with the use of echo planar and three-dimensional, fast spin echo techniques. *Occupational Health and Industrial Medicine*, 1(40):30, 1999.

[42] Canadian Centre for Occupational Health and Government of Canada Safety. Osh answers fact sheets. `http://www.ccohs.ca/oshanswers/phys_agents/exposure_can.html`.

[43] Jeffrey R Davis, Robert Johnson, and Jan Stepanek. *Fundamentals of Aerospace Medicine*. Lippincott Williams & Wilkins, 2008.

[44] Director General. Canada Occupational Health and Safety Regulations (SOR/86-304). RFC, Labour Program, April 2010.

[45] Anthony Faranesh. The interventional mri suite ismrm educational course, physics and techniques for clinicians. ISMRM 24th Annual Meeting and Exhibition, Singapore, 2016.

[46] Matthew Ethan MacDonald. *Passive Catheter Tracking into the Carotid Artery using Accelerated Magnetic Resonance Imaging*. PhD thesis, University of Calgary, 2010.

[47] Matthias Grothoff, Christopher Piorkowski, Thomas Gaspar, Sebastian Hilbert, Philipp Sommer, Steffen Weiss, Sascha Krüger, Tom Lloyd, Bernhard Schnackenburg, Gerhard Hindircks, et al. Comprehensive mri-guided intracardiac electrophysiological interventions in swine using a combination of active tracking and passive real-time catheter imaging. *Journal of Cardiovascular Magnetic Resonance*, 16(Suppl 1):O49, 2014.

[48] U Wonneberger, S Krüger, D Wirtz, C Leussler, S Weiss, K Jungnickel, M Ludewig, J Bunke, J Ricke, and F Fischbach. Clinically usable tool for dynamic scan-plane tracking for real-time mri-guided needle interventions in a high-field-open mri system. In *Proceeedings of the ISMRM 19th scientific meeting, Montreal*, volume 202, 2011.

[49] Jouke Smink, Marko Häkkinen, Ronald Holthuizen, Sascha Krueger, Mario Ries, Yasmina Berber, C Moonen, Max Köhler, and E Vahala. external control (xtc): a flexible, real-time, low-latency, bi-directional scanner interface. In *Proc Intl Soc Mag Reson Med*, volume 20, page 1755, 2011.

[50] Fabio Settecase, Alastair J Martin, Prasheel Lillaney, Aaron Losey, and Steven W Hetts. Magnetic resonance–guided passive catheter tracking for endovascular therapy. *Magnetic resonance imaging clinics of North America*, 23(4):591–605, 2015.

[51] MRI Real-Time. Real-time and interactive mri 13. *Intraoperative Imaging and Image-Guided Therapy*, page 193, 2014.

[52] Achieva release 3.2 series technical description. *4598 003 02911, 2012/06*, 2012.

[53] Matthew J Riffe, Stephen R Yutzy, Yun Jiang, Michael D Twieg, Colin J Blumenthal, Daniel P Hsu, Li Pan, Wesley D Gilson, Jeffrey L Sunshine, Christopher A Flask, et al. Device localization and dynamic scan plane selection using a wireless magnetic resonance imaging detector array. *Magnetic resonance in medicine*, 71(6):2243–2249, 2014.

[54] SP DiMaio, DF Kacher, RE Ellis, G Fichtinger, N Hata, GP Zientara, LP Panych, R Kikinis, and FA Jolesz. Needle artifact localization in 3t mr images. *Studies in health technology and informatics*, 119:120, 2006.

[55] Jeremy Cepek, Blaine A Chronik, and Aaron Fenster. The effects of magnetic field distortion on the accuracy of passive device localization frames in mr imaging. *Medical physics*, 41(5):052301, 2014.

[56] Junichi Tokuda, Sang-Eun Song, Gregory S Fischer, Iulian I Iordachita, Reza Seifabadi, Nathan B Cho, Kemal Tuncali, Gabor Fichtinger, Clare M Tempany, and Nobuhiko Hata. Preclinical evaluation of an mri-compatible pneumatic robot for angulated needle placement in transperineal prostate interventions. *International journal of computer assisted radiology and surgery*, 7(6):949–957, 2012.

[57] Gregory S Fischer, Simon P DiMaio, Iulian I Iordachita, and Gabor Fichtinger. Robotic assistant for transperineal prostate interventions in 3t closed mri. In *Medical Image Computing and Computer-Assisted Intervention–MICCAI 2007*, pages 425–433. Springer, 2007.

[58] Simon P DiMaio, Eigil Samset, G Fischer, Iulian Iordachita, Gabor Fichtinger, F Jolesz, and Clare M Tempany. Dynamic mri scan plane control for passive tracking of instruments and devices. In *Medical Image Computing and Computer-Assisted Intervention–MICCAI 2007*, pages 50–58. Springer, 2007.

[59] Ting Chen, Yiqiang Zhan, Shaoting Zhang, and Maneesh Dewan. Automatic alignment of brain mr scout scans using data-adaptive multi-structural model. In *Medical Image Computing and Computer-Assisted Intervention–MICCAI 2011*, pages 574–581. Springer, 2011.

[60] Benjamin Zaporzan, Adam C Waspe, Thomas Looi, Charles Mougenot, Ari Partanen, and Samuel Pichardo. Matmri and mathifu: software toolboxes for real-time monitoring and control of mr-guided hifu. *Journal of therapeutic ultrasound*, 1(1):1–12, 2013.

[61] Dibyadeep Nandi, Amira S Ashour, Sourav Samanta, Sayan Chakraborty, Mohammed AM Salem, and Nilanjan Dey. Principal component analysis in medical image processing: a study. *International Journal of Image Mining*, 1(1):65–86, 2015.

[62] Helen Xu, Andras Lasso, Peter Guion, Axel Krieger, Aradhana Kaushal, Anurag K Singh, Peter A Pinto, Jonathan Coleman, Robert L Grubb III, Jean-Baptiste Lattouf, et al. Accuracy analysis in mri-guided robotic prostate biopsy. *International journal of computer assisted radiology and surgery*, 8(6):937–944, 2013.

[63] T Carteret, M Merle, G Maclair, B denis de Senneville, C Moonen, and B Quesson. A rapid and robust method for reducing out-of-plane motion in dynamic imaging. application to mri thermometry on abdominal organs. ISMRM 17th Annual Meeting and Exhibition, Honolulu, Hawaii, 2009.

[64] Hervé Abdi and Lynne J Williams. Principal component analysis. *Wiley Interdisciplinary Reviews: Computational Statistics*, 2(4):433–459, 2010.

[65] Jan J Gerbrands. On the relationships between svd, klt and pca. *Pattern recognition*, 14(1):375–381, 1981.

[66] Stefan Van Der Walt, S Chris Colbert, and Gael Varoquaux. The numpy array: a structure for efficient numerical computation. *Computing in Science & Engineering*, 13(2):22–30, 2011.

[67] Vivek Kwatra and Mei Han. Fast covariance computation and dimensionality reduction for sub-window features in images. In *Computer Vision–ECCV 2010*, pages 156–169. Springer, 2010.

[68] Michael Holmes, Alexander Gray, and Charles Isbell. Fast svd for large-scale matrices. In *Workshop on Efficient Machine Learning at NIPS*, volume 58, pages 249–252, 2007.

[69] Fahit Gharibnezhad, Luis E Mujica, and José Rodellar. Applying robust variant of principal component analysis as a damage detector in the presence of outliers. *Mechanical Systems and Signal Processing*, 50:467–479, 2015.

[70] Omer Tamuz, Tsevi Mazeh, and Shay Zucker. Correcting systematic effects in a large set of photometric light curves. *Monthly Notices of the Royal Astronomical Society*, 356(4):1466–1470, 2005.

[71] Caroline D Jordan, Manojkumar Saranathan, Neal K Bangerter, Brian A Hargreaves, and Garry E Gold. Musculoskeletal mri at 3.0 t and 7.0 t: a comparison of relaxation times and image contrast. *European journal of radiology*, 82(5):734–739, 2013.

[72] M MacDonald, S Engler, AC Waspe, J Amaral, and S Pichardo. A simple mri scanner control technique for device localization during mri-guided interventions. In *Proc. of the ISMRM 24th Annual Meeting and Exhibition 2016; Singapore*, volume 3589, 2016.

[73] S Pichardo, Mougenot C, Engler S, AC Waspe, and J Drake. On demand reprogramming of mr sequence using matmri. In *Proc. of the ISMRM 24th Annual Meeting and Exhibition 2016; Suntec City, Singapore*, volume 3593, 2016.

[74] Thomas L Chenevert, Dariya I Malyarenko, David Newitt, Xin Li, Mohan Jayatilake, Alina Tudorica, Andriy Fedorov, Ron Kikinis, Tiffany Ting Liu, Mark Muzi, et al. Errors in quantitative image analysis due to platform-dependent image scaling. *Translational oncology*, 7(1):65–71, 2014.

[75] National Electrical Manufacturers Association, American College of Radiology, et al. *Digital imaging and communications in medicine (DICOM)*. National Electrical Manufacturers Association, 1998.

[76] Scott B Reeder, Bernd J Wintersperger, Olaf Dietrich, Titus Lanz, Andreas Greiser, Maximilian F Reiser, Gary M Glazer, and Stefan O Schoenberg. Practical approaches to the evaluation of signal-to-noise ratio performance with parallel imaging: Application with cardiac imaging and a 32-channel cardiac coil. *Magnetic Resonance in Medicine*, 54(3):748–754, 2005.

[77] Eunju Kim and Daehong Kim. Determining the location of metallic needle from mr images distorted by susceptibility difference. *Journal of the Korean Society of Magnetic Resonance in Medicine*, 14(2):87–94, 2010.

[78] PM Glover. Interaction of mri field gradients with the human body. *Physics in medicine and biology*, 54(21):R99, 2009.

[79] GE Healthcare. Mr echo demonstration. `https://www.youtube.com/watch?v=NnrZW5kBLDU`, May 11th, 2015.

[80] Heartvista Inc. Prescribing slices on the heartvista cardiac package. `https://www.youtube.com/watch?v=D_5odkO06cg`, October 6th, 2015.

[81] Samuel Pichardo, Max Köhler, Justin Lee, and Kullervo Hynnyen. In vivo optimisation study for multi-baseline mr-based thermometry in the context of hyperthermia using mr-guided high intensity focused ultrasound for head and neck applications. *International Journal of Hyperthermia*, 30(8):579–592, 2014.

[82] David Arthur and Sergei Vassilvitskii. k-means++: The advantages of careful seeding. In *Proceedings of the eighteenth annual ACM-SIAM symposium on Discrete algorithms*, pages 1027–1035. Society for Industrial and Applied Mathematics, 2007.

[83] Mandy Kaiser, Johannes Krug, and Georg Rose. Interventional mri: Minimal-invasive surgery under mr guidance. In *Microwave Symposium Digest (MTT), 2011 IEEE MTT-S International*, pages 1–4. IEEE, 2011.

[84] Hans-Martin Klein. Safety considerations. In *Clinical Low Field Strength Magnetic Resonance Imaging*, pages 35–47. Springer, 2016.

[85] Release of toshiba 3t mri system vantage titan 3t. Oct 2015.

[86] Michael J Lang, Alexander D Greer, and Garnette R Sutherland. *Intra-operative MRI at 3.0 Tesla: a Moveable Magnet*. Springer, 2011.

[87] Mark J White, John S Thornton, David J Hawkes, Derek LG Hill, Neil Kitchen, Laura Mancini, Andrew W McEvoy, Reza Razavi, Sally Wilson, Tarek Yousry, et al. Design, operation, and safety of single-room interventional mri suites: Practical experience from two centers. *Journal of Magnetic Resonance Imaging*, 41(1):34–43, 2015.

[88] Jian Yang and Jing-yu Yang. From image vector to matrix: a straightforward image projection techniqueimpca vs. pca. *Pattern Recognition*, 35(9):1997–1999, 2002.

[89] Claes Fornell, Byong-Duk Rhee, and Youjae Yi. Direct regression, reverse regression, and covariance structure analysis. *Marketing Letters*, 2(3):309–320, 1991.

[90] James Demmel, Ioana Dumitriu, and Olga Holtz. Fast linear algebra is stable. *Numerische Mathematik*, 108(1):59–91, 2007.